# Multiple Equidistant Belt Technique for Width Function Estimation through A Two-Segmented-Distance Strategy

Pengfei Wu<sup>1</sup>, Jintao Liu<sup>1</sup>, Meiyan Feng<sup>1</sup>, and Hu Liu<sup>2</sup>

<sup>1</sup>Hohai University

<sup>2</sup>Northwest Institute of Eco-Environment and Resources, Chinese Academy of Sciences

February 20, 2023

#### Abstract

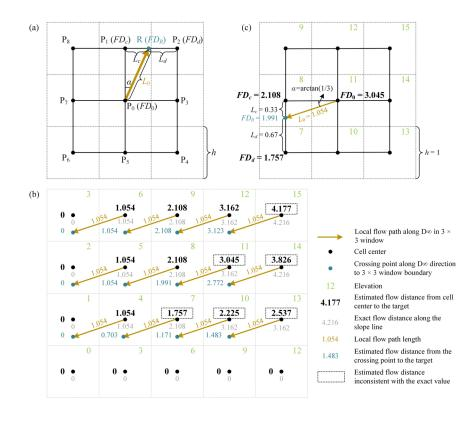
The arbitrary adoption of cell center to represent the whole cell is a compromise to the grid structure of the digital elevation models (DEMs), which greatly limits the accuracy of estimating flow distance and width functions. This study uses the triangulation with linear interpolation (TLI) method to approximate the missing flow distance values within a cell except for the cell center. A new flow distance algorithm (D[?]-TLI) is proposed to improve the flow distance estimation by using a two-segment-distance strategy. The first segment distance from a cell center to a crossing point at the local  $3 \times 3$  window boundary is modeled by the D[?] method. The second segment distance souring from the crossing point is estimated by the TLI using the flow distance values assigned for the two closest downstream cell centers, while these values have been assigned by iterating from lowest to highest cells. Then, using the continuous flow distance field approximated over a cell region, this cell can be divided into multiple equidistant belts (MEB) to estimate the width function. Four numerical terrains and two real-world terrains are used for assessments. The results demonstrate that D[?]-TLI outperforms nine existing flow distance algorithms over any numerical terrains, and it is overall optimal for real-world terrains. Meanwhile, MEB extracts the width function which is less affected by unreasonable artificial fluctuation than the previous method. Hence, MEB combined with D[?]-TLI can obtain a high-accuracy estimation of hydro-geomorphological attributes that may be conducive to the application of hydrologic modeling.

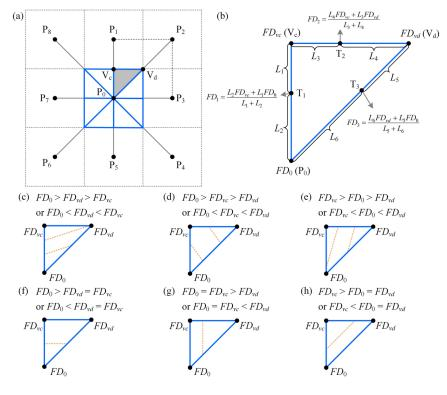
#### Hosted file

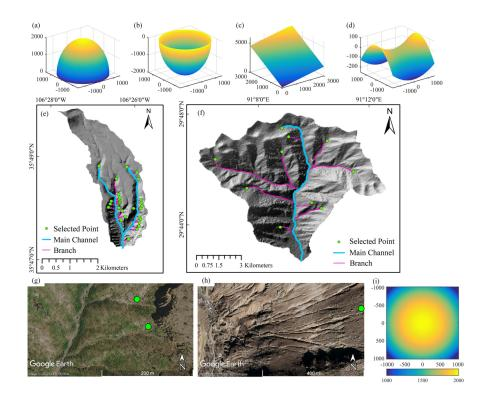
955816\_0\_art\_file\_10686706\_rppv9y.docx available at https://authorea.com/users/546750/ articles/625179-multiple-equidistant-belt-technique-for-width-function-estimationthrough-a-two-segmented-distance-strategy

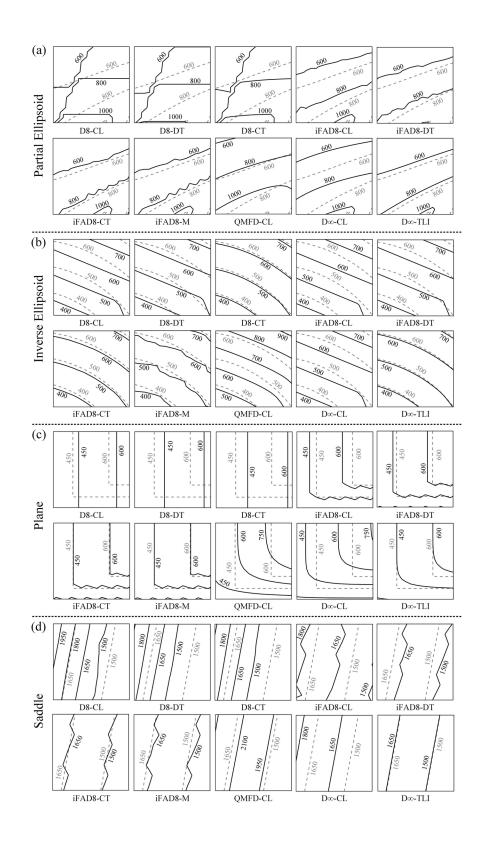
#### Hosted file

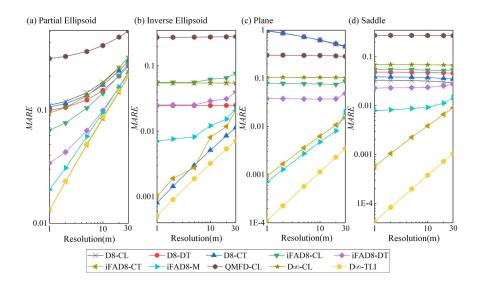
955816\_0\_supp\_10686741\_rpptt0.docx available at https://authorea.com/users/546750/articles/ 625179-multiple-equidistant-belt-technique-for-width-function-estimation-through-a-twosegmented-distance-strategy

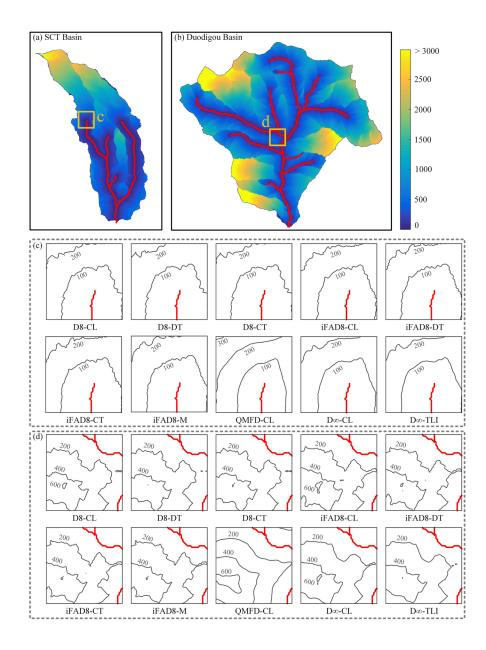


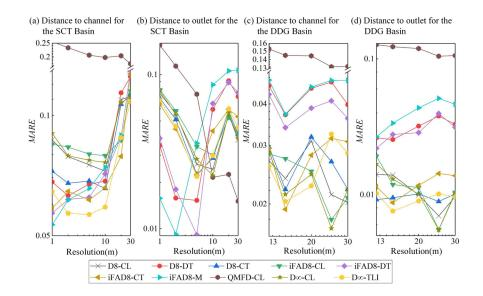


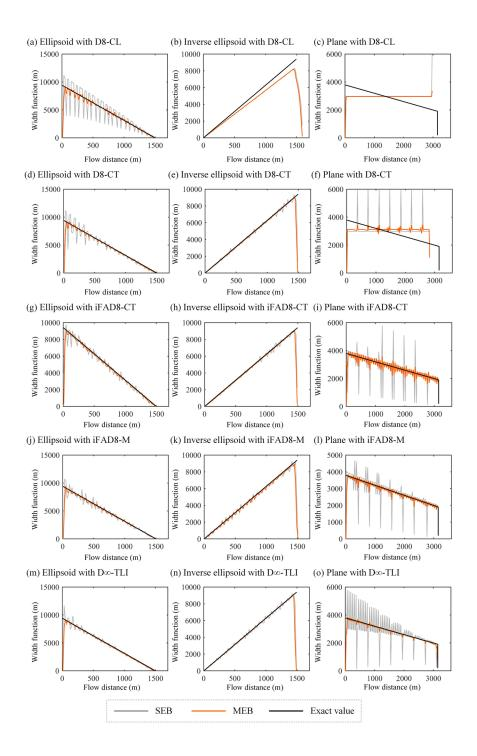


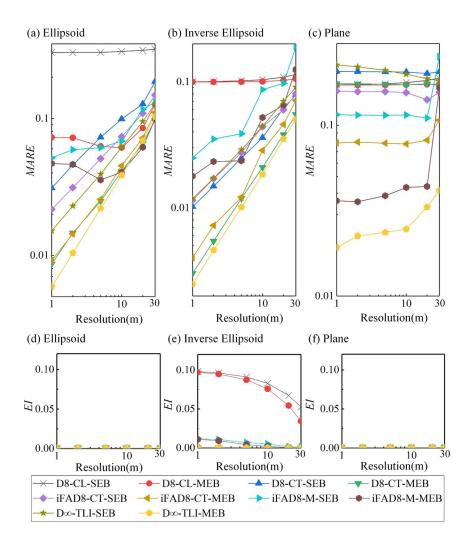


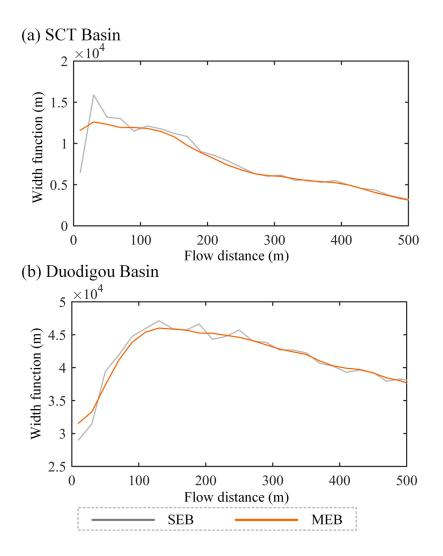












1	Multiple Equidistant Belt Technique for Width Function
2	Estimation through A Two-Segmented-Distance Strategy
3	
4	Pengfei Wu <sup>1,2</sup> , Jintao Liu <sup>1,2*</sup> , Meiyan Feng <sup>1,2</sup> , Hu Liu <sup>3</sup>
5	
6	<sup>1</sup> State Key Laboratory of Hydrology-Water Resources and Hydraulic Engineering,
7	Hohai University, Nanjing 210024, China
8	<sup>2</sup> College of Hydrology and Water Resources, Hohai University, Nanjing 210024,
9	China
10	<sup>3</sup> Linze Inland River Basin Research Station, Chinese Ecosystem Research Network,
11	Lanzhou 730000, China
12	
13	* Corresponding author: jtliu@hhu.edu.cn (J. Liu).
14	

# 15 Key Points

16 Triangulation with linear interpolation (TLI) is adopted to approximate the flow

17 distance values for a cell region except for its center.

- 18 Two segmented-distances inside and outside a local 3 × 3 window are severally
- 19 modeled by  $D\infty$  and TLI.
- 20 Estimation of width function can be essentially improved with possible multiple
- 21 equidistant belts technique over a cell.

22

## 23 Abstract

24 The arbitrary adoption of cell center to represent the whole cell is a compromise to the 25 grid structure of the digital elevation models (DEMs), which greatly limits the 26 accuracy of estimating flow distance and width functions. This study uses the 27 triangulation with linear interpolation (TLI) method to approximate the missing flow 28 distance values within a cell except for the cell center. A new flow distance algorithm 29  $(D\infty$ -TLI) is proposed to improve the flow distance estimation by using a 30 two-segment-distance strategy. The first segment distance from a cell center to a 31 crossing point at the local  $3 \times 3$  window boundary is modeled by the D $\infty$  method. The 32 second segment distance souring from the crossing point is estimated by the TLI using 33 the flow distance values assigned for the two closest downstream cell centers, while 34 these values have been assigned by iterating from lowest to highest cells. Then, using 35 the continuous flow distance field approximated over a cell region, this cell can be 36 divided into multiple equidistant belts (MEB) to estimate the width function. Four 37 numerical terrains and two real-world terrains are used for assessments. The results 38 demonstrate that  $D\infty$ -TLI outperforms nine existing flow distance algorithms over any 39 numerical terrains, and it is overall optimal for real-world terrains. Meanwhile, MEB 40 extracts the width function which is less affected by unreasonable artificial fluctuation 41 than the previous method. Hence, MEB combined with Do-TLI can obtain a 42 high-accuracy estimation of hydro-geomorphological attributes that may be conducive 43 to the application of hydrologic modeling.

# 44 Keywords

- 45 Flow distance; Width function; Two-segmented-distance strategy; Triangulation with
- 46 linear interpolation; Multiple equidistant belt technique

47

### 48 **1. Introduction**

49 As an important feature of overland flow, flow distance is essential for hydrological, geomorphological, and ecological research, such as runoff or flood analysis (Bogaart 50 51 & Troch, 2006; Di Lazzaro et al., 2016; Liu et al., 2012; McGuire et al., 2005; Muzik, 1996; Rinaldo et al., 1991; Xu et al., 2018), soil erosion or thickness simulation 52 53 (Dong et al., 2022; Hickey, 2000; Tesfa et al., 2009), and water quality modeling (Fan 54 et al., 2015). These researches rely on flow distance estimations with different scales, 55 including distance to channel or outlet (Bogaart & Troch, 2006; Van Nieuwenhuizen, 2021), river length (Fan et al., 2015) and uphill slope line length (Dong et al., 2022; 56 Tesfa et al., 2009). Meanwhile, as a form of flow distance distribution, width function 57 58 of a hillslope or catchment is always used as a hydrologic response function in 59 hydrologic modeling (Bogaart & Troch, 2006; Gupta et al., 1986; Hazenberg et al., 60 2015; Lapides et al., 2022; Liu et al., 2016; Moussa, 2008; Noël et al., 2014; Ranjram 61 & Craig, 2021; Rigon et al., 2016; Troch et al., 2002, 2003). Thus, there has been 62 renewed interest in algorithms to accurately estimate flow distance as well as width 63 function.

As the discretized representation of terrains by the grid digital elevation models (DEMs), flow distance is always estimated by cumulating the length along the predicted DEM-<u>based flow path</u> (Mayorga et al., 2005). Flow path, according to whether a cell is allowed to drain to more than one downslope cell, can be estimated by two types of flow direction algorithms, i.e., the single flow direction (SFD) algorithms and the multiple flow direction (MFD) algorithms (Wilson et al., 2007). The SFD path uses a zigzag line whose flow distance can be measured explicitly. However, the MFD path is a dispersive network whose flow distance must be computed implicitly as the weighted average length of all the lines based on the flow proportion distributed from the beginning cell along every line (Bogaart & Troch, 2006).

75 Once the spatial distribution of flow distance is computed, the width function can 76 always be estimated implicitly (e.g., Liu et al., 2012; Sahoo & Sahoo, 2019b). In this 77 implicit method, the width function is defined as an area distribution function (Moussa, 2008; Veneziano et al., 2000) or probability density function (Bogaart & 78 79 Troch, 2006; Liu et al., 2012; Sahoo & Sahoo, 2019a, 2019b) of the equidistant belts. 80 Compared with the explicit method that directly considers contour lengths as width 81 functions (Fan & Bras, 1998), the implicit method is more suitable for applications in 82 the real-world hillslopes or catchments (Sahoo & Sahoo, 2019b). Moreover, it can 83 provide width functions with more details when compared with the strategies which obtain monotonic width functions by simplifying the terrains into regular shapes (e.g., 84 85 Noël et al., 2014).

However, the discretized grid structure of DEM has naturally limited the accuracy of the predicted flow path, it thus further constrains the precision of the flow distance estimation as well as the width function estimation (Liu et al., 2012; Paik, 2008; Paz et al., 2008; Wu et al., 2020). For instance, most flow direction algorithms were designed to fix the flow path out from a local cell center down to one or more other downstream cell centers (e.g., O'Callaghan & Mark, 1984; Quinn et al., 1991;

92	Orlandini et al., 2003; Shin & Paik, 2017; Tarboton, 1997; Paik, 2008; Wu et al.,
93	2020), but the true path may miss these centers (Paik, 2008). So, the flow distance
94	along a predicted flow path to a given target may be inconsistent with the true flow
95	distance (Paz et al., 2008; Liu et al., 2012). A solution to this problem is to employ
96	some highly accurate flow direction algorithms to track the gravity-driven flow path
97	which is essentially not forced to pass the downstream cell centers (e.g., Zhou et al.,
98	2011). However, this solution does not apply to large scales because the related flow
99	direction algorithms require vast computing time as well as storage space (Zhou et al.,
100	2011).
101	In order to ensure acceptable computational efficiency, the flow distance assignment
102	for each cell center is better to only search in a local window rather than the whole
103	flow path. Bogaart and Troch (2006) proposed such a two-segmented-distance
104	framework which only models the sub-distance from the cell center to a crossing point
105	at a $3 \times 3$ window boundary and adds it to the sub-distance sourcing from the crossing
106	point to a given target (e.g., channel) for the final flow distance value. But this method
107	only adopted center-to-center flow path previously because the true crossing points
108	inconsistent with cell centers may be not assigned with flow distance values, although
109	some strategies can restore the true sub-distance in the $3 \times 3$ window accurately (e.g.,
110	Butt & Maragos, 1998; De Smith, 2004; Liu et al., 2012; Paz et al., 2008). Hence, the
111	lack of flow distance values at a cell region except for its center seems to limit the
112	improvements in flow distance estimation.

113 Meanwhile, the missing flow distance values prevent it from dividing a cell covering

multiple equidistant belts into correct numbers of belts. So the conventional method adds the whole cell into merely one equidistant belt based on the flow distance value assigned for the cell center. Then imprecise equidistant belt area function will lead to width function with unreasonable artificial fluctuation because some equidistant belts may capture too many regions from adjacent belts as shown in the results of some existing studies (e.g., Moussa, 2008; Liu et al., 2012; Sahoo & Sahoo, 2019b; Veneziano et al., 2000).

121 In fact, following common geographical studies, the missing flow distance values at a 122 cell region except for its center can be approximated using the values assigned to cell 123 centers with an interpolation method (e.g., Lee & Schachter, 1980; Polidori & 124 Chorowicz, 1993; Schwendel et al., 2012; Yilmaz, 2007). However, there is no 125 existing study trying to adopt the interpolation method to improve the accuracy of 126 flow distance estimation as well as width function estimation. Hence, this study 127 attempts to incorporate an interpolation method, i.e., the triangulation with linear 128 interpolation (TLI) method (Sloan, 1987; Yilmaz, 2007), into the flow distance 129 algorithm and the width function algorithm for better estimation accuracy. Here TLI is 130 selected firstly because of its high precision (Schwendel et al., 2012). In addition, TLI 131 can provide straight isolines in a cell region, dividing the cell into regular equidistant 132 belts whose area can be measured explicitly for the width function. Finally, both the 133 numerical and the real-world terrains with different resolutions are adopted for the 134 comparison between the proposed and the existing algorithms.

#### 135 **2. Methodology and Experiments**

#### 136 **2.1. Flow Distance Estimation Combining D** $\infty$ **And TLI**

137 The new flow distance algorithm requires a DEM with flats and depressions removed. 138 Each cell center at the channel network or any other given target such as outlet is 139 assigned with a flow distance value equal to zero. Then all the cells without flow 140 distance values are sorted into a queue in an ascending elevation order, and the flow 141 distances from cell centers in the queue are calculated with elevation from low to high. 142 This framework inherited from the method by Bogaart and Troch (2006) can 143 guarantee that flow distances from all the neighboring downstream cell centers 144 surrounding the current cell to channel are known. The cells with the same elevation 145 can be processed in an arbitrary order because the flow will not be drained to a 146 neighboring cell with the same elevation when the flats are removed.

147 Figure 1a shows a sketch to calculate the flow distance from a cell center ( $P_0$ ) to 148 channel (or other target). Firstly, a  $3 \times 3$  window is built using the current cell and its 149 eight neighbors. The D $\infty$  method proposed by Tarboton (1997) is adopted for the local 150 flow path in the window following some existing literature (Liu et al., 2012; Orlandini 151 et al., 2003; Shin & Paik, 2017). Then the crossing point (i.e., R) along the local flow 152 path to the window boundary can be identified. Based on the  $D\infty$  theory, the closest 153 cardinal and diagonal neighboring cell centers (i.e., P<sub>1</sub> and P<sub>2</sub> in Figure 1a) to R are always lower than P<sub>0</sub>, so they have been assigned with flow distance values according 154 to the framework iterating from low to high. 155

156 Although TLI cannot provide the whole flow distance distribution in the window

before the assignment of flow distance for  $P_0$ , it can assign the flow distance value for any point on the line  $P_1P_2$  with the existing flow distance values assigned for these two cell centers. The flow distance (*FD<sub>R</sub>*) from R to channel is computed by TLI as following:

$$FD_R = \frac{L_d F D_c + L_c F D_d}{L_c + L_d} \tag{1}$$

where  $FD_c$  and  $FD_d$  denote the flow distance from the nearest cardinal cell center (i.e., P<sub>1</sub>) and the nearest diagonal cell center (i.e., P<sub>2</sub>) to channel, respectively.  $L_c$  and  $L_d$ denote the length from R to the nearest cardinal cell center (i.e., P<sub>1</sub>) and the nearest diagonal cell center (i.e., P<sub>2</sub>), respectively.  $L_c$  and  $L_d$  can be calculated as following:

$$L_c = h \tan \alpha \tag{2}$$

167 
$$L_d = h(1 - \tan \alpha) \tag{3}$$

168 where *h* denotes the resolution of DEM, and  $\alpha$  denotes the angle between the D $\infty$ 169 direction and the closest cardinal direction. There is a special case when the D $\infty$ 170 direction points to a neighboring cell center. In this case, the other nearest cell center 171 may be higher than P<sub>0</sub>, and here its flow distance value is unknown. It makes no 172 difference because *FD<sub>R</sub>* is equal to the flow distance value assigned for the cell center 173 pointed by the D $\infty$  direction according to Equation 1 in this case. Then the local flow 174 path length (*L*<sub>0</sub>) by D $\infty$  is calculated as:

175 
$$L_0 = \frac{h}{\cos\alpha} \tag{4}$$

176 Finally, the flow distance  $(FD_0)$  from P<sub>0</sub> to channel is defined as:

$$FD_0 = FD_R + L_0 \tag{5}$$

178 This new algorithm combines  $D\infty$  and TLI, so it is referred as  $D\infty$ -TLI. A DEM of a

plane with a gradient ratio of 3:1 is provided as an example in Figure 1b to show the capacity of  $D\infty$ -TLI to restore the flow distance to the DEM side. The estimated local flow path length, as well as both the estimated flow distances from the crossing point and the cell center to the DEM side, is labelled for each cell in Figure 1b. Moreover, an enlarged 3 × 3 window in Figure 1c is used to show the detailed assignment of flow distance for a cell center following Equation 1-5.

185 According to the estimated flow distance distribution (black values) in Figure 1b, the 186 difference between the estimated flow distance and the exact slope line length is little 187 for most cell centers. Here the exact slope line originating from a cell center is 188 consistent with the gravity-driven flow path (Maxwell, 1870; Orlandini et al., 2014). 189 This example only shows the potential of  $D\infty$ -TLI to provide the flow distance 190 distribution for the plane. However, whether more bias may appear when  $D\infty$ -TLI is 191 applied to other terrains (e.g., divergent, or convergent terrains) still needs further 192 verifications. Hence, multiple terrains (see in section 2.3.1) with different 193 complexities are adopted to assess  $D\infty$ -TLI in our experiments.

### 194 **2.2. Width Function Calculation with TLI**

The width function coincides with the area distribution function of equidistant belt (Moussa, 2008), so the proposed algorithm extracts the equidistant belt firstly. In this step, cells in the specific hillslope or catchment are processed one by one. For each cell, the proposed algorithm firstly obtains the equidistant lines whose flow distances to channel are multiple to the belt interval, then each area between two equidistant lines is added to the corresponding equidistant belt. Here the belt interval is always set to be the DEM resolution (e.g., Liu et al., 2012; Moussa, 2008; Sahoo & Sahoo,
202 2019b).

203 To implement above scheme, according to some existing flow direction algorithms 204 (e.g., Pilesjö & Hasan, 2014; Tarboton, 1997), a given cell is firstly divided into eight 205 triangular facets as marked in blue in Figure 2a. Then every facet is processed 206 independently. The grey facet in Figure 2a is taken for illustration. There are two 207 vertexes (i.e.,  $V_c$  and  $V_d$ ) except the current cell center (i.e.,  $P_0$ ) within this facet.  $V_c$  is 208 the midpoint of the given cell center ( $P_0$ ) and its cardinal neighbor center ( $P_1$  for the 209 selected facet), and  $V_d$  is the midpoint of the given cell center (P<sub>0</sub>) and its diagonal 210 neighbor center ( $P_2$  for the selected facet).

Equidistant lines (dotted lines in Figure 2c-2h) should be obtained firstly. However, if any one of the neighboring cells (i.e.,  $P_1$  or  $P_2$ ) belong to another hillslope or catchment, this facet will not be further divided to avoid the effects of unreasonable critical lines. Then this facet is added to the belt covering the flow distance from the cell center ( $P_0$ ). This step ensures that the integration of the width function is equal to the area of the extracted hillslope or catchment.

When all the three vertexes belong to the same hillslope or catchment, the continuous flow distance field for the facet is calculated using the TLI method. Here the flow distance from P<sub>0</sub>, P<sub>1</sub>, P<sub>2</sub>, P<sub>3</sub> are expressed as  $FD_0$ ,  $FD_1$ ,  $FD_2$ ,  $FD_3$ , and the mean of these four flow distance values is expressed as MD. According to the TLI, the flow distance from V<sub>c</sub> to channel (i.e.,  $FD_{vc}$ ) can be calculated following:

222 
$$FD_{\nu c} = (FD_0 + FD_1)/2$$
 (6)

223 According to Zhou et al. (2011) method, the flow distance from V<sub>d</sub> to channel (i.e.,

224  $FD_{vd}$ ) is calculated as below:

225 
$$FD_{vd} = \begin{cases} (FD_1 + FD_3)/2, & if |MD - (FD_1 + FD_3)/2| \le |MD - (FD_0 + FD_2)/2| \\ (FD_0 + FD_2)/2, & if |MD - (FD_1 + FD_3)/2| > |MD - (FD_0 + FD_2)/2| \end{cases}$$
226 (7)

227 Then the equations for the flow distance from any point at the facet sides to channel 228 are shown in Figure 2b. These equations can also help to obtain the point position at a 229 side with a given flow distance. Thus, when the given flow distance ranges between 230 the minimum and the maximum flow distances from the three vertexes, only two 231 points owning the given distance can be found at the three sides, and the equidistant 232 line can be approximated by a straight line linking them (Figure 3c-3h). When the 233 flow distances from the three vertexes to channel are different from each other, one 234 point must be located on the side whose two vertexes own the minimum and the 235 maximum flow distances respectively, and the second point can be located on one of 236 the other two sides (Figure 3c-3e). Otherwise, the equidistant line should be parallel to 237 the side linking two vertexes whose flow distances are equal (Figure 3f-3h). 238 Thereupon, the facet can be divided into multiple equidistant belts between the 239 equidistant lines.

After all the cells in the hillslope or catchment are processed, the probability density (p(x)) and the area distribution of equidistant belt are generated. Here the width of every equidistant belt is the ratio of the equidistant belt area (Sp(x)) to the belt interval ( $L_u$ ), i.e.,  $Sp(x)/L_u$ , and is defined as the width at the middle flow distance of the belt, where S is the total area of the hillslope or catchment. Hence, the applications of area distribution and probability density function to obtain the width function are consistent. This proposed division method for width function is referred as the multiple equidistant belt (MEB) method, which is different from the conventional method adds a cell into single equidistant belt (SEB).

#### 249 **2.3. Experiment Materials and Assessment Criteria**

#### 250 **2.3.1. Numerical and Real-world Terrains**

251 Four numerical terrains and two real-world terrains are adopted for algorithm 252 assessments (Figure 3). The numerical terrains contain an ellipsoid, an inverse 253 ellipsoid, a plane, and a saddle (Figure 3a-3d). These terrains represent the divergent, 254 the convergent, the plain and the complex terrains, respectively. The formulas 255 proposed by Li et al. (2021) are used to build these terrains with six resolutions (1 m, 256 2 m, 5 m, 10 m, 20 m, 30 m). As mentioned in Section 2.1, the exact flow distance is 257 equal to the slope line length for the numerical terrains. This length can be calculated 258 by integration using the slope line formulas introduced by Li et al. (2021), and then 259 the exact equidistant belt area can be divided for the exact width function. When 260 assessing the flow distance algorithms, only the partial ellipsoid with a square 261 boundary in Figure 3i is used because there is a systematic error between the circle 262 boundary of the complete ellipsoid and the valid DEM cells (Figure S1). But the 263 assessments of the width function use the complete ellipsoid because it is hard to 264 obtain the exact equidistant line or belt with integration when only the partial terrain 265 is used. The saddle is not employed for the width function extraction due to the lack 266 of the exact equidistant belt area.

It is difficult to obtain the exact flow distances from most positions over a real-world terrain to channel or outlet. However, flow distance from a point in a channel or gully can be measured along the overland flow trajectory. So, some channels (or gullies) in two real-world terrains, including a sub-basin of the Spruce Canyon (Figure 3e) and the Duodigou Basin (Figure 3f), are mapped using the images from the Google Earth for the assessments (e.g., Figure 3g and 3h).

273 The Spruce Canyon is in New Mexico, USA, while the selected tributary sub-basin (referred as SCT Basin) owns a drainage area of 7.0 km<sup>2</sup> with the elevation ranging 274 275 from 2292 m to 3027 m. This basin has a relatively low mean slope  $(17.2^{\circ})$ , while the 276 valley bottoms and the channels are narrower than 100 m and 3 m, respectively. The 277 downstream channels of thirty points are mapped. To avoid repetitive computation 278 bias, only two longest channels are selected as the main channels, while other 279 twenty-eight channels end up at the main channel and are regarded as branches. The 280 lengths of two main channels are 3475 m and 3496 m, while the lengths of the 281 branches range from 75 m to 687 m. Bare earth DEM data with 1 m resolution is 282 provided by the Jemez River Basin Snow-off LiDAR Survey, and is resampled to five 283 coarser resolutions (2 m, 5 m, 10 m, 20 m, 30 m) consistent with the selected 284 resolutions of the numerical terrains.

The Duodigou Basin (referred as DDG Basin) is in the Tibetan Plateau, China (Fei et al., 2022). It is a steep alpine terrain covering 56.6 km<sup>2</sup> with the elevation ranging from 3719 m to 5425 m and the mean slope equal to  $28.0^{\circ}$ . The valley bottom is narrow (< 20 m) at upstream and wide (> 900 m) at downstream. The downstream channels of ten points are mapped. The longest channel (11386 m) is selected as the main channel. The lengths of the branches range from 936 m to 5979 m. These channels are narrower than 10 m. The 12.5 m-resolution DEM of this basin is obtained from the Advanced Land Observing Satellite (ALOS). Limited by the coarse initial resolution, the DEM is resampled to four resolutions (15 m, 20 m, 25 m, 30 m) with smaller intervals than those of other terrains to show the influence of the resolution.

#### 296 **2.3.2. Algorithm Assessments**

297 Ten flow distance algorithms including  $D\infty$ -TLI and nine other algorithms are adopted 298 to assess the estimated flow distance distribution over the numerical and the 299 real-world terrains, and their information are listed in Table 1. Here the traditional 300 cumulative length (CL) method, the distance transform (DT) method by Paz et al. 301 (2008), and the cosine transform (CT) method by Liu et al. (2012) are combined with 302 two SFD algorithms, i.e., the classical D8 algorithm (O'Callaghan & Mark, 1984) and 303 a highly accurate algorithm named iFAD8 (Wu et al., 2020). The merging (M) method 304 by Dong et al. (2022) is also employed and combined with iFAD8. The cumulative 305 length methods based on  $D\infty$  and QMFD proposed by Bogaart and Troch (2006) are 306 also adopted. Hence, ten algorithms for comparison are D8-CL, D8-DT, D8-CT, 307 iFAD8-CL, iFAD8-DT, iFAD8-CT, iFAD8-M, D∞-CL, QMFD-CL and D∞-TLI. The 308 flow direction algorithms (D8, iFAD8,  $D\infty$  and QMFD) are selected due to their 309 applicability for flow distance measurements. Although some other flow direction 310 algorithms are shown to be more effective in other applications (e.g., Pilesjö & Hasan,

2014; Wu et al., 2022), they are not suitable to this study because they provide flowpath out from a non-point source.

The mean absolute relative error (*MARE*) is used to assess the deviations between the estimated and the exact flow distances, which is defined as follows:

$$RE_i = \frac{PV_i - EV_i}{EV_i} \tag{8}$$

316 
$$MARE = \frac{1}{n} \sum_{i=1}^{n} |RE_i|$$
(9)

where  $PV_i$  and  $EV_i$  are the estimated and the exact values of the *i*th cell, respectively.  $RE_i$  denotes the relative error of the *i*th cell, and *n* denotes the number of cells considered for the assessment.

320 When width function is estimated for a terrain, the exact widths of some estimated 321 equidistant belts may be zero due to the possible overestimation of the flow distance. 322 This phenomenon can limit the direct application of MARE to assess the deviations 323 between the estimated and the exact width functions. Hence, two valid assessment 324 criteria are adopted here. Firstly, a part of the equidistant belts with flow distances not 325 exceeding the maximum exact flow distance are selected to calculate the MARE 326 following Equation 8 and 9. Here  $PV_i$  and  $EV_i$  in Equation 8 are the *i*th estimated and 327 the *i*th exact widths, respectively. Then the exceeding index (EI) is adopted to 328 represent the ratio of the widths whose estimated flow distances are longer than the 329 exact maximum flow distance.

$$EI = \frac{\sum_{j=1}^{m} W_j}{T}$$
(10)

where *m* denotes the number of the equidistant belts exceeding the maximum exact flow distance, and  $W_j$  denotes the *j*th exceeding equidistant belt width. *T* denotes the total width of all exact equidistant belts. It is obvious that an accurate width function
should possess both low *MARE* and *EI* values.

**335 3. Results** 

#### **336 3.1. Assessments of the Flow Distance Algorithms**

#### **337 3.1.1. Performances over the Numerical Terrains**

338 To show the difference between the exact and the estimated flow distance distribution clearly, the partial enlarged details over the 20 m-resolution terrains are shown in 339 340 Figure 4. Meanwhile, the flow distance distributions over the whole terrains are 341 provided in Figure S2. According to Figure 4b and 4d,  $D\infty$ -TLI can reproduce the 342 exact flow distance correctly for the inverse ellipsoid and the saddle. The isolines of 343 flow distance by  $D\infty$ -TLI are smooth and parallel to the exact isolines over the partial ellipsoid, while the deviation of D∞-TLI is as low as iFAD8-CT or iFAD8-M (Figure 344 345 4a). However, D∞-TLI underestimates the flow distance where the exact isolines 346 facing two directions intersect over the plane (see in Figure 4c). For other algorithms, 347 the results by the D8-based algorithms (including D8-CL, D8-DT and D8-CT) are 348 unreasonable.  $D\infty$ -CL and QMFD-CL overestimate flow distance everywhere. 349 Although iFAD8-CL and iFAD8-DT lead to large deviations over all the numerical 350 terrains, the other two iFAD8-based algorithms (iFAD8-CT and iFAD8-M) can 351 reproduce the exact flow distance distribution more reasonably than other algorithms 352 except D<sub>∞</sub>-TLI. But the accuracy of iFAD8-CT or iFAD8-M is unsteady as shown by 353 the undulant isolines, and it is obviously lower than the accuracy of D∞-TLI over the inverse ellipsoid and the saddle. Hence,  $D\infty$ -TLI is shown to be the best choice to 354

reproduce flow distance distributions over the numerical terrains based on the visual
assessments, which is also proven by the results over 5 m-resolution terrains (Figure
S3).

According to the quantitative assessments (Figure 5), lower MARE appears when a 358 359 finer resolution is used for most cases. Do-TLI is shown to outperform other 360 algorithms because it obtains the least MAREs with all resolutions over the inverse 361 ellipsoid, the plane or the saddle, while only iFAD8-CT has a similar great 362 performance with  $D\infty$ -TLI over the partial ellipsoid. Overall, the average MARE of 363 D∞-TLI is only 2.31 % over four numerical terrains. iFAD8-CT and iFAD8-M are the two algorithms only second to  $D\infty$ -TLI, and have obvious improvements to 364 iFAD8-CL and iFAD8-DT while iFAD8-DT outperforms iFAD8-CL. D8-DT and 365 366 D8-CT outperform D8-CL over the partial ellipsoid and the inverse ellipsoid, but 367 underperform D8-CL over the saddle. The D8-based algorithms have similar 368 performances over the plane. Consistent with the results in Figure 4, D∞-CL and 369 QMFD-CL obtain great errors over all the terrains, and  $D\infty$ -CL seems to be more 370 accurate than QMFD-CL.

#### 371 **3.1.2. Real-world Applications**

The distribution of flow distance to the mapped channels is calculated in both the SCT Basin and the DDG Basin, and the visual results by different algorithms are shown in Figure 6. Here some short channels in the SCT Basin are ignored and only four channels are adopted. Enlarged details in Figure 6c and 6d show that the MFD-based algorithms including D $\infty$ -TLI, D $\infty$ -CL and QMFD-CL provide smoother isolines of flow distance than the selected seven SFD-based algorithms. Compared with other algorithms,  $D\infty$ -CL and QMFD-CL always overestimate the flow distance. The strategy DT, CT and M can shorten the results of CL no matter which SFD algorithm (D8 or iFAD8) is selected, which is shown clearly by the isoline of 100 m over the SCT Basin (Figure 6c) and the isoline of 600 m over the DDG Basin (Figure 6d).

382 Two cases are considered for the quantitative assessments, i.e., the flow distances 383 from the selected points to the main channels shown in Figure 3e and 3f, as well as 384 the flow distances from all the selected points to the basin outlet. The wavy MAREs 385 show that the ability of every selected algorithm is unsteady over the real-world terrains with different resolutions (Figure 7). However, compared with other 386 387 algorithms, D $\infty$ -TLI can always obtain acceptable *MAREs*. For any case in Figure 7, 388 the average *MARE* of all the resolutions is listed in Table 2. D $\infty$ -TLI is always one of 389 the three best choices for any case. In addition, the average MARE of all the cases and 390 resolutions are calculated, and the value of  $D\infty$ -TLI (4.01 %) is the lowest, while the 391 values of D8-CT (4.30 %) and iFAD8-CT (4.29 %) are lower than other algorithms 392 except  $D\infty$ -TLI. The average *MAREs* of QMFD-CL are too high over the real-world 393 terrains. The performances of D8-CL, D8-DT, iFAD8-CL, iFAD8-M and D∞-CL are 394 similar according to the results in Table 2.

#### **395 3.2. Assessments of the Width Function**

According to the results in Section 3.1, only five flow distance algorithms are selected to provide the flow distance distribution for the width function algorithm assessments, including  $D\infty$ -TLI, classical D8-CL, and three algorithms with acceptable performances over the numerical or the real-world terrains (i.e., D8-CT, iFAD8-CT
and iFAD8-M). Figure 8 shows the width functions estimated by two width function
algorithms (i.e., the conventional SEB and the proposed MEB) with different
estimated flow distance distributions over three 20 m-resolution numerical terrains.
Here the flow distance interval of the equidistant belt for the width function is equal to
the DEM resolution (i.e., 20 m) following some existing studies (e.g., Liu et al., 2012;
Moussa, 2008; Sahoo & Sahoo, 2019b).

406 As shown in Figure 8, while the exact width functions for the numerical terrains are 407 smooth, SEB causes artificial fluctuations for the estimated width functions in most 408 cases. The MEB algorithm can decrease these unreasonable artificial fluctuations 409 successfully. The quantitative assessment results in Figure 9 also show that MEB 410 improves the accuracy of the estimated width function with the lower MARE than 411 SEB for any selected flow distance distribution. Meanwhile, EI is always equal to 412 zero over the ellipsoid or the plane, and slightly larger than zero over the inverse ellipsoid when the flow distance distribution by D8-CL or iFAD8-M is adopted. The 413 414 estimated width function combining MEB and D<sup>∞</sup>-TLI is highly consistent with the 415 exact width function (Figure 8m-8o), and generally obtains the lowest MARE over all 416 the numerical terrains (Figure 9). The average MARE is 2.97 % for this combination 417 but higher than 5% for other combinations. Other estimated flow distance 418 distributions except the distribution by D∞-TLI can restore the trend of the exact 419 width function over the ellipsoid with SEB or MEB (Figure 8a, 8d, 8g and 8j). 420 However, the deviation of D8-CL is great over the inverse ellipsoid (Figure 8b) and 421 the plane (Figure 8c), while the deviation of D8-CT is great over the plane (Figure 8f).

422 These unreasonable deviations can also be identified from Figure 9.

423 The application over the real-world terrain also shows that MEB can overcome the 424 artificial fluctuations (Figure 10). To obtain the exact width function over a real-world 425 terrain is a great challenge. However, if the flow distance to channel is close to zero, 426 the estimated width can be assumed to be double the channel length because the 427 equidistant belt has a small interval and is close to both the channel banks. This is not 428 a very disciplined assessment method, but can provide a reference for the application 429 over the real-world terrain. Here the SCT Basin with 1 m-resolution DEM is selected 430 for real-world applications and the width function to channel (including four channels 431 in Figure 6a) with an equidistant belt interval of 1 m is calculated. No matter which 432 algorithm is adopted to determine the flow distance distribution, the area of the first 433 equidistant belt with flow distance ranging from 0 m to 1 m should be much smaller 434 than the exact area as shown in Figure 8. This is because the exact first equidistant 435 belt is covered by both the hillslope and the channel cells while the proposed 436 algorithm only estimates width function using the hillslope cells. Hence, the next belt 437 ranging from 1 m to 2 m (i.e., the width at 1.5 m flow distance) is used to predict the 438 total channel length (7546 m), and the results are shown in Table 3.

The relative errors of all the predicted lengths by SEB exceed 10 %, while the relative errors by MEB are lower than 10 %. Combined with MEB, the relative errors of  $D\infty$ -TLI and D8-CL are lower than 3 %. Meanwhile, Table 3 shows the widths at three neighboring flow distances (i.e., 1.5 m, 2.5 m, 3.5 m) by different combinations. Although slight fluctuation in width function is normal, the fluctuation of the selected
widths by any SEB-based combination is too strong for such a small flow distance
interval. This unreasonable fluctuation is obviously artificial which is caused by SEB.

446 **4. Discussions** 

#### 447 **4.1. Different Algorithms on Flow Distance Estimation Accuracy**

448 The flow direction algorithm selected seems to be the major influence factor to the 449 accuracy according to the results in Section 3.1. All the D8-based algorithms (i.e., 450 D8-CL, D8-DT and D8-CT) provides abnormal flow distance distributions over the 451 partial ellipsoid, the plane and the saddle, but more effective distributions over the 452 inverse ellipsoid (Figure 4). This is because D8 can provide false flow paths directing 453 the flow to incorrect targets over the divergent and the plain terrains, but has an 454 acceptable performance over the convergent terrain (Wu et al., 2022). Meanwhile, 455 D8-CL and D8-CT can provide reasonable flow distances to outlet for the selected 456 points over two selected real-world terrains (Table 2), because most portion of the 457 flow path from a selected point to the outlet is in the convergent valley where the D8 458 algorithm works effectively.

iFAD8 can provide reasonable zigzag flow paths out from the cell center (Wu et al., 2020), so the results by any iFAD8-based algorithm (i.e., iFAD8-CL, iFAD8-DT, iFAD8-CT and iFAD8-M) can approximately reflect the features of the exact flow distance distributions. D $\infty$  and QMFD provide dispersive flow paths and may drain a part of the flow into the channel at some unusually distant locations, so D $\infty$ -CL and QMFD-CL always overestimate the flow distance (Figure 4 and 6). D $\infty$  is less 465 dispersive than QMFD (Orlandini et al., 2012), so  $D\infty$ -CL obtains better results than 466 QMFD-CL over all the terrains. Generally, the SFD-based algorithms get better 467 application results than the existing MFD-based algorithms (i.e.,  $D\infty$ -CL and 468 QMFD-CL).

469 D $\infty$ -TLI outperforms any other selected algorithm by estimating the generally most 470 accurate flow distance over both the numerical and the real-world terrains. Although 471 the traditional D $\infty$  method is treated as a MFD method, D $\infty$ -TLI neglects the 472 dispersive global flow path of D $\infty$  and only employs D $\infty$  for the local drainage 473 direction. Hence, D $\infty$ -TLI does not suffer the serious problem of dispersive flow path 474 by the MFD methods and can provide more accurate flow distance.

475 There are some strategies to improve the precision of the local drainage direction by 476  $D\infty$  (e.g., Hooshyar et al., 2016; Wu et al., 2020). These new methods may obtain the 477 potential to further improve the accuracy of the estimated flow distance. But when the 478 new infinite direction (ND $\infty$ ) method proposed by Wu et al. (2020) is adopted to replace the  $D\infty$  direction in  $D\infty$ -TLI, no obvious improvement appears to the accuracy 479 480 over the real-world terrains (Figure S4). That is because the limited improvement of 481 ND $\infty$  to D $\infty$  can be offset by other errors, such as the errors in TLI or the DEM 482 generation. Hence, the applicability of the improved strategies to  $D\infty$  requires more 483 assessments in further studies, and the tradition  $D^{\infty}$  direction is recommended in this 484 study due to its simplicity and popularization.

#### 485 **4.2. Width Function Estimation**

486 It is possible that some cells cover multiple equidistant belts when their cell centers

487	are located on the same equidistant belt. Then SEB adds all these cell areas into one
488	equidistant belt while other neighboring equidistant belts receive no cell area, which
489	draws the artificial fluctuations in Figure 8. The originality of MEB is to attempt to
490	divide a cell into correct equidistant belts, so it is unsurprising to find that MEB leads
491	to slighter artificial fluctuation. However, the accuracy of the estimated width
492	function depends not only on the width function algorithm (i.e., SEB or MEB), but
493	also on the selected flow distance algorithm. With a specific flow distance distribution,
494	MEB can estimated the width function more accurately than SEB (Figure 9). For a
495	specific width function algorithm (SEB or MEB), its accuracy can be greatly
496	improved by using a more accurate flow distance algorithm. However, the
497	combination of SEB with a more accurate flow distance algorithm may outperform
498	the combination of MEB with a flow distance algorithm of which the accuracy is not
499	that high. As an instance, iFAD8-CT causes higher MARE than iFAD8-M when
500	providing flow distance distribution for the plane (Figure 5c), but iFAD8-CT-MEB
501	obtains a better width function than iFAD8-M-SEB (Figure 9c). While $D\infty$ -TLI is
502	shown to be the best choice for flow distance estimation, the combination of $D\infty$ -TLI
503	with MEB is optimal, which is demonstrated by the steady great performance over the
504	numerical and the real-world terrains (Figure 9 and Table 3).
505	The nexulta in Section 2.2 are based on a traditional meson dition that the actuidistant

The results in Section 3.2 are based on a traditional precondition that the equidistant belt interval for the width function is equal to the DEM resolution. This is a small interval, so the region not belonging to the correct equidistant belt may occupy a large proportion of the whole cell region. This precondition may increase the artificial fluctuation. If the interval is set to be larger, more area in a cell can belong to the same equidistant belt as the cell center, then the SEB method will suffer a slighter artificial fluctuation. However, MEB can still optimize the accuracy of SEB to a degree in this case as shown in Figure S5.

513 **4.3. Computational Efficiency** 

514 All the flow distance algorithms used in this study are implemented following the 515 two-segmented-distance strategy. The runtimes for the plane with different resolutions 516 show that this strategy can guarantee acceptable computational efficiency (Table 4). D $\infty$ -TLI can process a DEM with more than  $9 \times 10^6$  cells in less than 20.0 s. This 517 518 runtime is similar to  $D\infty$ -CL, and is longer than the D8-based algorithms as well as 519 QMFD-CL, while is shorter than the iFAD8-based algorithms. This is similar to the 520 difference in efficiency of the selected flow direction algorithms (D8, iFAD8,  $D\infty$  and 521 QMFD) as shown by Wu et al. (2022). So, the selected flow direction algorithm seems 522 to be the main factor affecting runtime. The computation efficiency of MEB is also 523 acceptable with less than 14.0 s required to process the same 1 m-resolution DEM 524 using any given flow distance distribution. This runtime is much longer than the SEB 525 algorithm (0.08 s), but is shorter than the runtimes of most flow distance algorithms.

526

#### **5. Concluding Remarks**

527 A new method to estimate flow distance, as well as width function based on grid 528 DEMs, is proposed in this study. The new flow distance algorithm (D $\infty$ -TLI) adopts a 529 two-segmented-distance strategy that divides the flow distance into two segments 530 whose sub-distances are approximated using D $\infty$  and TLI, respectively. Then, the

532

continuous flow distance field is approximated over each cell region, so this cell area can be divided into multiple equidistant belts (MEB) for the width function.

533 Four numerical terrains and two real-world terrains with multiple resolutions are 534 adopted for assessments. The results show that  $D\infty$ -TLI generally outperforms nine 535 existing flow distance algorithms and causes low average MAREs of 2.31 % and 4.01% 536 for the estimated flow distance distribution over the numerical and the real-world 537 terrains, respectively. Compared with the traditional method, MEB can effectively 538 decrease the artificial fluctuations in the estimated width function. The combination of 539  $D\infty$ -TLI with MEB (i.e.,  $D\infty$ -TLI-MEB) outperforms other combinations by 540 providing estimated width functions with an average MARE of 2.97 % for the 541 numerical terrains, while it also works well over real-world terrains. Meanwhile, all 542 the strategies used in this study (including the two-segmented-distance strategy, 543  $D\infty$ -TLI, and MEB) show acceptable computational efficiency. Therefore,  $D\infty$ -TLI 544 and MEB have great potential to provide hydro-geomorphological attributes for 545 hydrological models.

In further studies, more experiments can be conducted to show how much our method can improve hydrological modeling, although the numerical accuracy advantage of the flow distance and width function estimated by the newly proposed method has been provided here.  $D\infty$  and TLI are selected here due to their great accuracy in common geographical studies, but the performance of other local drainage direction methods and interpolation methods can be tested and evaluated by replacing  $D\infty$  or TLI in this method.

## 553 Acknowledgements

This work was supported by the Second Tibetan Plateau Scientific Expedition and Research Program (STEP; grant no. 2019QZKK0207-02), the National Natural Science Foundation of China (NSFC; grant no. 92047301), and the Postgraduate Research & Practice Innovation Program of Jiangsu Province (grant no. KYCX22 0636).

559 **Open Research** 

## 560 Data and Code Availability Statement

The DEMs of the numerical terrains available 561 are at: 562 https://doi.org/10.6084/m9.figshare.16909321.v1 (Wu et al., 2022). The DEM 563 containing the SCT Basin distributed by OpenTopography is available at: 564 https://doi.org/10.5069/G9RB72JV. The ALOS DEM containing the DDG Basin is 565 available at: https://search.earthdata.nasa.gov. The real-world basin domains as well 566 as the mapped channels are available at: 567 https://doi.org/10.6084/m9.figshare.22004444.v1. The Java codes of the proposed 568 algorithms are available at: https://doi.org/10.6084/m9.figshare.22010132.v1.

- 569 **References**
- 570 Bogaart, B. W., & Troch, P. A. (2006). Curvature distribution within hillslopes and 571 catchments and its effect on the hydrological response. *Hydrology and Earth*
- 572 System Sciences, 10, 925-936. https://doi.org/10.5194/hess-10-925-2006
- 573 Butt, M. A., & Maragos, P. (1998). Optimum design of chamfer distance transforms.
- 574 IEEE Transactions on Image Processing, 7(10), 1477-1484.

- 575 https://doi.org/10.1109/83.718487
- 576 De Smith, M. (2004). Distance transforms as a new tool in spatial analysis, urban
- 577 planning, and GIS. Environment and Planning B: Planning and Design, 31(1),
- 578 85-104. https://doi.org/10.1068/b29123
- 579 Di Lazzaro, M., Zarlenga, A., & Volpi, E. (2016). Understanding the relative role of
- dispersion mechanisms across basin scales. *Advances in Water Resources*, *91*,
  23-36. http://doi.org/10.1016/j.advwatres.2016.03.003
- 582 Dong, L., Ge, C., Zhang, H., Liu, Z., Yang, Q., Jin, B., Ritsema, C. J., & Geissen, V.
- (2022). An optimized method for extracting slope length in RUSLE from raster
  digital elevation. *Catena*, 209, 105818.
  https://doi.org/10.1016/j.catena.2021.105818
- 586 Fan, Y., & Bras, R. L. (1998). Analytical solutions to hillslope subsurface storm flow
- and saturation overland flow. *Water Resources Research*, 34, 921-927.
  https://doi.org/10.1029/97WR03516
- 589 Fan, F. M., Fleischmann, A. S., Collischonn, W., Ames, D. P., & Rigo, D. (2015).
- 590 Large-scale analytical water quality model coupled with GIS for simulation of
- 591 point sourced pollutant discharges. Environmental Modelling & Software, 64,
- 592 58-71. http://doi.org/10.1016/j.envsoft.2014.11.012
- 593 Fei, J., Liu, J., Ke, L., Wang, W., Wu, P., & Zhou, Y. (2022). A deep learning-based
- 594 method for mapping alpine intermittent rivers and ephemeral streams of the
- 595 Tibetan Plateau from Sentinel-1 time series and DEMs. *Remote Sensing of*
- 596 *Environment*, 282, 113271. https://doi.org/10.1016/j.rse.2022.113271

- 597 Gupta, V., Waymire, E., & Rodíguez-Iturbe, I. (1986). On scales, gravity and network
- 598 structure in basin runoff. In Gupta, V., Waymire, E., & Rodíguez-Iturbe, I. (Eds),
- 599 Scale Problems in Hydrology (pp. 159-184). D. Reidel Publishing Co.
   600 http://doi.org/10.1007/978-94-009-4678-1 8
- Hazenberg, P., Fang, Y., Broxton, P., Gochis, D., Niu, G. Y., Pelletier, J. D., Troch, P.
- A., & Zeng, X. (2015). A hybrid-3D hillslope hydrological model for use in
- Earth system models. *Water Resources Research*, 51, 8218-8239.
- 604 https://doi.org/10.1002/2014WR016842
- Hickey, R. (2000). Slope angle and slope length solutions for GIS. *Cartography*, 29(1),
- 606 1-8. https://doi.org/10.1080/00690805.2000.9714334
- 607 Hooshyar, M., Wang, D., Kim, S., Medeiroset, S. C., & Hagen, S. C. (2016). Valley
- and channel networks extraction based on local topographic curvature and k-
- means clustering of contours. *Water Resources Research*, 52, 8081-8102.
- 610 https://doi.org/10.1002/2015WR018479
- 611 Lapides, D., Sytsma, A., O'Neil, G., Djokic, D., Nichols, M., & Thompson, S. (2022).
- 612 Arc Hydro Hillslope and Critical Duration: New tools for hillslope-scale runoff
- 613 analysis. Environmental Modelling and Software, 153, 105408.
- 614 https://doi.org/10.1016/j.envsoft.2022.105408
- 615 Lee, D. T., & Schachter, B. J. (1980). Two algorithms for constructing a Delaunay
- 616 triangulation. International Journal of Computer & Information Sciences, 9(3),
- 617 219-242. https://doi.org/10.1007/BF00977785
- 618 Li, Z., Yang, T., Wang, C., Shi, P., Yong, B., & Song, Y. (2021). Assessing the

- 619 precision of total contributing area (TCA) estimated by flow direction algorithms
- based on the analytical solution of theoretical TCA on synthetic surfaces. *Water*
- 621 *Resources Research*, 57, e2020WR028546.
- 622 https://doi.org/10.1029/2020WR028546
- Liu, J., Chen, X., Zhang, X., & Hoagland, K. D. (2012). Grid digital elevation model
  based algorithms for determination of hillslope width functions through flow
  distance transforms. *Water Resources Research*, 48, W04532.
  http://doi.org/10.1029/2011WR011395
- Liu, J., Han, X., Chen, X., Lin, H., & Wang, A. (2016). How well can the subsurface
  storage-discharge relation be interpreted and predicted using the geometric
  factors in headwater areas?. *Hydrological Processes*, 30(25), 4826-4840.
- 630 https://doi.org/10.1002/hyp.10958
- Maxwell, J. C. (1870). On hills and dales. *The London, Edinburgh, and Dublin Philosophical Magazine and Journal of Science*, 40(269), 421-427.
- Mayorga, E., Logsdon, M. G., Ballester, M., & Richey, J. E. (2005). Estimating
  cell-to-cell land surface drainage paths from digital channel networks, with an
  application to the amazon basin. *Journal of Hydrology*, 315, 167-182.
- 636 http://doi.org/10.1016/j.jhydrol.2005.03.023
- 637 McGuire, K. J., McDonnell, J. J., Weiler, M., Kendall, C., McGlynn, B. L., Welker, J.
- M., & Seibert, J. (2005). The role of topography on catchment-scale water
  residence time. *Water Resources Research*, 41, W05002.
- 640 http://doi.org/10.1029/2004WR003657

- 641 Moussa, R. (2008). What controls the width function shape, and can it be used for
- 642 channel network comparison and regionalization?. *Water Resources Research*, 44,
- 643 W08456. http://doi.org/10.1029/2007WR006118
- 644 Muzik, I. (1996). Flood modelling with GIS-derived distributed unit hydrographs.
- *Hydrological Processes*, *10*, 1401-1409.
  https://doi.org/10.1002/(SICI)1099-1085(199610)10:10<1401::AID-HYP469>3.
  0.CO;2-3
- Noël, P., Rousseau, A. N., Paniconi, C., & Nadeau, D. F. (2014). Algorithm for
  delineating and extracting hillslopes and hillslope width functions from gridded
  elevation data. *Journal of Hydrologic Engineering*, 19(2), 366-374.
  https://doi.org/10.1061/(ASCE)HE.1943-5584.0000783
- 652 O'Callaghan, J. F., & Mark, D. M. (1984). The extraction of drainage networks from
- digital elevation data. Computer Vision, Graphics, and Image Processing, 28(3),

654 323-344. https://doi.org/10.1016/S0734-189X(84)80011-0

- 655 Orlandini, S., Moretti, G., Corticelli, M. A., Santangelo, P. E., Capra, A., Rivola, R., &
- Albertson, J. D. (2012). Evaluation of flow direction methods against field
- observations of overland flow dispersion. Water Resources Research, 48,
- 658 W10523. https://doi.org/10.1029/2012WR012067
- 659 Orlandini, S., Moretti, G., Franchini, M., Aldighieri, B., & Testa, B. (2003).
- 660 Path-based methods for the determination of nondispersive drainage directions in
- grid-based digital elevation models. *Water Resources Research*, 39(6), 1144.
- 662 https://doi.org/10.1029/2002WR001639

- Orlandini, S., Moretti, G., & Gavioli, A. (2014). Analytical basis for determining
  slope lines in grid digital elevation models. *Water Resources Research*, 50,
- 666 Paik, K. (2008). Global search algorithm for nondispersive flow path extraction.

526-539. https://doi.org/10.1002/2013WR014606

- 667 Journal of Geophysical Research, 113, F04001.
   668 https://doi.org/10.1029/2007JF000964
- 669 Paz, A. R., Collischonn, W., Risso, A., & Mendes, C. A. B. (2008). Errors in river
- 670 lengths derived from raster digital elevation models. *Computers & Geosciences*,
- 671 *34*, 1584-1596. https://doi.org/10.1016/j.cageo.2007.10.009
- Pilesjö, P., & Hasan, A. (2014). A triangular form-based multiple flow algorithm to
  estimate overland flow distribution and accumulation on a digital elevation
  model. *Transactions in GIS*, *18*(1), 108-124. https://doi.org/10.1111/tgis.12015
- 675 Polidori, L., & Chorowicz, J. (1993). Comparison of bilinear and Brownian
- 676 interpolation for digital elevation models. *ISPRS Journal of Photogrammetry and*
- 677 *Remote Sensing*, 48(2), 18-23. https://doi.org/10.1016/0924-2716(93)90036-m
- 678 Quinn, P., Beven, K., Chevallier, P., & Planchon, O. (1991). The prediction of
- hillslope flow paths for distributed hydrological modelling using digital terrain
  models. *Hydrological Processes*, 5, 59-79.
- 681 https://doi.org/10.1002/hyp.3360050106
- Ranjram, M., & Craig, J. R. (2021). Use of an efficient proxy solution for the
  hillslope-storage Boussinesq problem in upscaling of subsurface stormflow. *Water Resources Research*, 57, e2020WR029105.

### 685 https://doi.org/10.1029/2020WR029105

- 686 Rigon, R., Bancheri, M., Formetta, G., & de Lavenne, A. (2016). The 687 geomorphological unit hydrograph from a historical-critical perspective. Earth 688 Surface Processes and Landforms, 41, 27-37. https://doi.org/10.1002/esp.3855 689 Rinaldo, A., Marani, A., & Rigon, R. (1991). Geomorphological dispersion. Water 690 Resources Research, 27(4), 513-525. https://doi.org/10.1029/90WR02501 691 Sahoo, S., & Sahoo, B. (2019a). A geomorphology-based integrated stream-aquifer 692 interaction model for semi-gauged catchments. Hydrological Processes, 33, 693 1362-1377. https://doi.org/10.1002/hyp.13406 694 Sahoo, S., & Sahoo, B. (2019b). Modelling the variability of hillslope drainage using 695 grid-based hillslope width function estimation algorithm. ISH Journal of 696 Hydraulic Engineering, 25(1), 71-78. 697 https://doi.org/10.1080/09715010.2018.1441750 698 Schwendel, A. C., Fuller, I. C., & Death, R. G. (2012). Assessing DEM interpolation 699 methods for effective representation of upland stream morphology for rapid 700 appraisal of bed stability. River Research and Applications, 28(5), 567-584. 701 https://doi.org/10.1002/rra.1475 702 Shin, S., & Paik, K. (2017). An improved method for single flow direction calculation 703 in grid digital elevation models. Hydrological Processes, 31(8), 1650-1661.
- 704 https://doi.org/10.1002/hyp.11135
- Sloan, S. W. (1987). A fast algorithm for constructing Delaunay triangulations in the
- plane. Advances in Engineering Software, 9(1), 34-55.

707	Tarboton, D. G. (1997). A new method for the determination of flow directions and
708	upslope areas in grid digital elevation models. Water Resources Research, 33(2),
709	662-319. https://doi.org/10.1029/96WR03137

- 710 Tesfa, T. K., Tarboton, D. G., Chandler, D. G., & McNamara, J. P. (2009), Modeling
- soil depth from topographic and land cover attributes. *Water Resources Research*,

712 *45*, W10438. https://doi.org/10.1029/2008WR007474

- 713 Troch, P. A., Paniconi, C., & van Loon, E. E. (2003). Hillslope-storage Boussinesq
- model for subsurface flow and variable source areas along complex hillslopes: 1.
- formulation and characteristic response. *Water Resources Research*, *39*(11), 1316.
- 716 https://doi.org/10.1029/2002WR001728
- 717 Troch, P., van Loon, E., & Hilberts, A. (2002). Analytical solutions to a
- hillslope-storage kinematic wave equation for subsurface flow. Advances in
- 719 Water Resources, 25, 637-649. https://doi.org/10.1016/S0309-1708(02)00017-9
- 720 Van Nieuwenhuizen, N., Lindsay, J. B., & DeVries, B. (2021). Smoothing of digital
- elevation models and the alteration of overland flow path length distributions.
- 722 *Hydrological Processes*, *35*(7), e14271. https://doi.org/10.1002/hyp.14271
- 723 Veneziano, D., Moglen, G. E., Furcolo, P., & Iacobelli, V. (2000). Stochastic model of
- the width function. *Water Resources Research*, 36(7), 1143-1157.
   https://doi.org/10.1029/2000WR900002
- 726 Wilson, J. P., Lam, C. S., & Deng, Y. (2007). Comparison of the performance of
- flow-routing algorithms used in GIS-based hydrologic analysis. *Hydrological*
- 728 Processes, 21, 1026-1044. https://doi.org/10.1002/hyp.6277

- Wu, P., Liu, J., Han, X., Feng, M., Fei, J., & Shen, X. (2022). An improved triangular
- form-based multiple flow direction algorithm for determining the nonuniform
- flow domain over grid networks. Water Resources Research, 58,
- 732 e2021WR031706. https://doi.org/10.1029/2021WR031706
- 733 Wu, P., Liu, J., Han, X., Liang, Z., Liu, Y., & Fei, J. (2020). Nondispersive drainage
- direction simulation based on flexible triangular facets. *Water Resources Research*, 56, e2019WR026507. https://doi.org/10.1029/2019WR026507
- 736 Yilmaz, H. M. (2007). The effect of interpolation methods in surface definition: an
- experimental study. Earth Surface Processes and Landforms, 32, 1346-1361.
- 738 https://doi.org/10.1002/esp.1473
- 739 Xu, H., Ma, C., Lian, J., Xu, K., & Evance, C. (2018). Urban flooding risk assessment
- based on an integrated k-means cluster algorithm and improved entropy weight
- method in the region of Haikou, China. Journal of Hydrology, 563, 975-986.
- 742 https://doi.org/10.1016/j.jhydrol.2018.06.060
- 743 Zhou, Q., Pilesjö, P., & Chen, Y. (2011). Estimating surface flow paths on a digital
- elevation model using a triangular facet network. *Water Resources Research*, 47,
- 745 W07522. https://doi.org/10.1029/2010WR009961

# 746 Tables

Algorithm	Origin of the cumulative	Adopted flow direction	Origin of the flow direction algorithm		
Aigoituini	distance algorithm	algorithm			
D8-CL	-	D8	O'Callaghan and Mark (1984)		
D8-DT	Paz et al. (2008)	D8	O'Callaghan and Mark (1984)		
D8-CT	Lin $at al (2012)$	$D8 / D\infty$	O'Callaghan and Mark (1984)		
D8-C1	Liu et al. (2012)	$D8 / D\infty$	/ Tarboton (1997)		
iFAD8-CL	-	iFAD8	Wu et al. (2020)		
iFAD8-DT	Paz et al. (2008)	iFAD8	Wu et al. (2020)		
EADS OT	$L_{1}^{2} = 4 + 1 + (2012)$		Wu et al. (2020) / Tarboton		
iFAD8-CT	Liu et al. (2012)	iFAD8 / D∞	(1997)		
iFAD8-M	Dong et al. (2022)	iFAD8	Wu et al. (2020)		
QMFD-CL	Bogaart and Troch (2006)	QMFD	Quinn et al. (1991)		
D∞-CL	Bogaart and Troch (2006)	$D\infty$	Tarboton (1997)		
D∞-TLI	Current study	$D\infty$	Tarboton (1997)		

747 **Table 1.** The flow distance algorithms adopted for the comparison in this study.

748	Table 2. The ave	rage MARE of the	e estimated flow	distance by	different algorithms.

	D8-CL	D8-DT	D8-CT	iFAD8-CL	iFAD8-DT	iFAD8-CT	iFAD8-M	QMFD-CL	D∞-CL	D∞-TLI
Distance to channel for the SCT Basin	8.93	8.44	8.24	8.84	7.84	7.62	7.92	21.26	9.04	7.22
Distance to outlet for the SCT Basin	4.58	4.81	4.52	4.94	4.93	4.78	5.99	6.71	4.65	4.52
Distance to channel for the DDG Basin	2.61	4.32	2.79	2.48	3.93	2.94	4.65	14.31	2.52	2.57
Distance to outlet for the DDG Basin	1.09	3.09	0.96	1.17	2.99	1.20	4.03	11.59	1.12	0.93
All the cases above	4.49	5.29	4.30	4.57	5.04	4.29	5.72	13.47	4.50	4.01

*Note.* The unit is in  $10^{-2}$ , and the three lowest average *MAREs* of every case are bolded.

751	Table 3. Relative errors between the exact length and the predicted river lengths using the equidistant belt areas by different flow distance
752	algorithms and width function extraction modes.

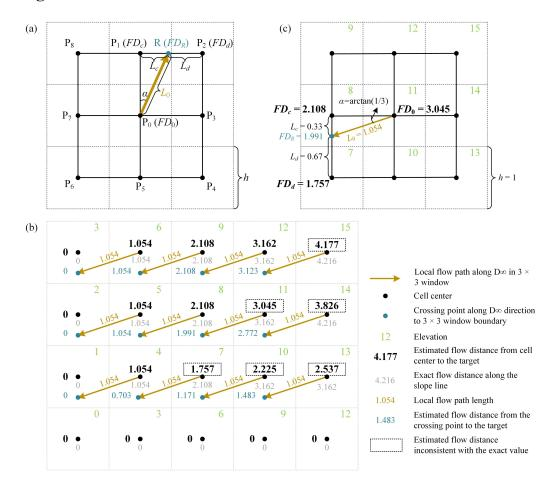
algorithmis and w	Taur Tanetic									
	D8-CL-SEB	D8-CL-MEB	D8-CT-SEB	D8-CT-MEB	iFAD8-CT-SEB	iFAD8-CT-MEB	iFAD8-M-SEB	iFAD8-M-MEB	D∞-TLI-SEB	D∞-TLI-MEB
Width at distance of 1.5 m										
(m)	17683	15425	18514	15779	18343	16129	17633	15682	18222	15471
Width at distance of 2.5 m										
(m)	19731	16118	18123	16546	17994	16745	21262	18300	17528	16277
Width at distance of 3.5 m										
(m)	17288	16091	16198	16521	16792	16770	17065	16840	17538	16278
Predicted river length (m)	8842	7712	9257	7889	9172	8064	8817	7841	9111	7736
Relative error (%)	17.17	2.21	22.67	4.55	21.54	6.87	16.84	3.91	20.74	2.51

Resolution	Cell	Do ot	DO DT	D. CT	TADA GI		ELDO CE	T. DOM		D GI	
(m)	Numbers	D8-CL	D8-DT	D8-CT	iFAD8-CL	iFAD8-DT	iFAD8-CT	iFAD8-M	QMFD-CL	D∞-CL	D∞-TLI
30	$1.02 \times 10^{4}$	0.003	0.004	0.007	0.012	0.015	0.017	0.01	0.005	0.008	0.007
20	2.28×10 <sup>4</sup>	0.01	0.008	0.017	0.027	0.025	0.037	0.02	0.009	0.022	0.018
10	9.06×10 <sup>4</sup>	0.043	0.042	0.064	0.113	0.108	0.137	0.093	0.046	0.068	0.067
5	3.61×10 <sup>5</sup>	0.198	0.227	0.324	0.513	0.551	0.632	0.459	0.269	0.33	0.318
2	2.25×10 <sup>6</sup>	2.097	2.155	2.877	4.379	4.583	5.181	5.554	2.378	2.775	2.895
1	9.01×10 <sup>6</sup>	11.562	10.306	16.936	21.513	24.577	27.01	59.79	13.971	17.333	18.401

**Table 4.** The runtimes of different flow distance algorithms to process the plane with different resolutions.

*Note.* The unit is in second. The evaluation is performed on a computer with an Intel Xeon E5-1620 v4 CPU and 80 GB of memory.

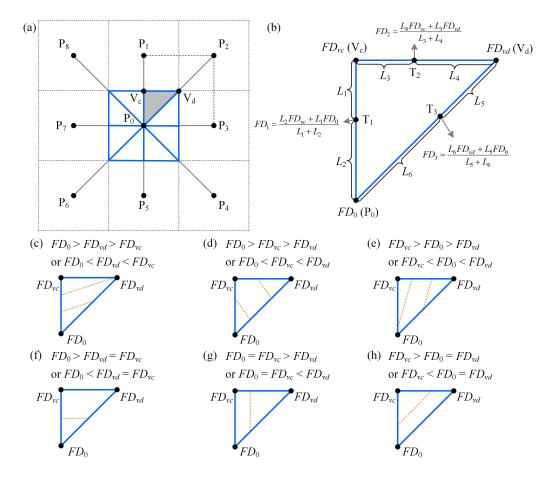
## 757 Figures



758

Figure 1. The theory of the new flow distance algorithm. (a) Flow distance  $(FD_0)$ 759 760 from a cell center ( $P_0$ ) to a downstream target is computed as the sum of the local flow path length ( $L_0$ ) along D $\infty$  direction in a 3  $\times$  3 window and the estimated flow distance 761 762 from the crossing point (R) on the window boundary to the same target. (b) A 1 763 m-resolution DEM of a plane is adopted as an example. Then the estimated 764 distribution of flow distance to DEM side for the cell centers as well as the data 765 generated in the computational process are shown. The exact flow distances which is 766 calculated as the lengths of theoretical slope lines are also shown. Meanwhile, (c) shows the process of the flow distance value assignment for the cell center whose 767

relevation is equal to 11.



770

Figure 2. The method to determine the local equidistant belt area which is used to constitute the width function. (a) The cell is divided into eight facets as shown with blue boundary, and the flow distance of any point at the facet boundary can be calculated following (b), where  $L_1, ..., L_6$  denote the lengths from the points to the vertexes. (c-h) Each equidistant line is straight and linking two points at the boundary with the same flow distance, and the area between two equidistant lines is added to the corresponding equidistant belt.

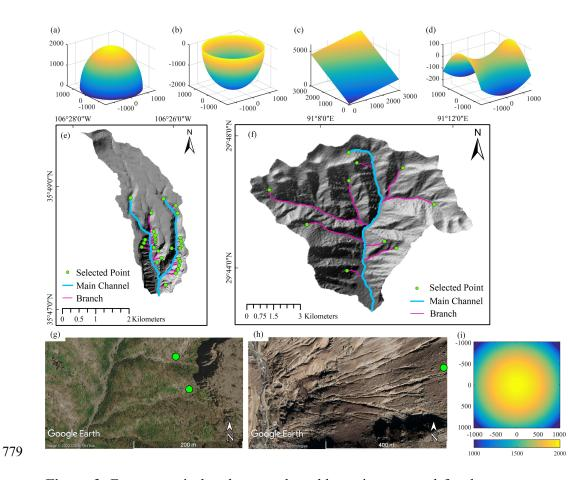
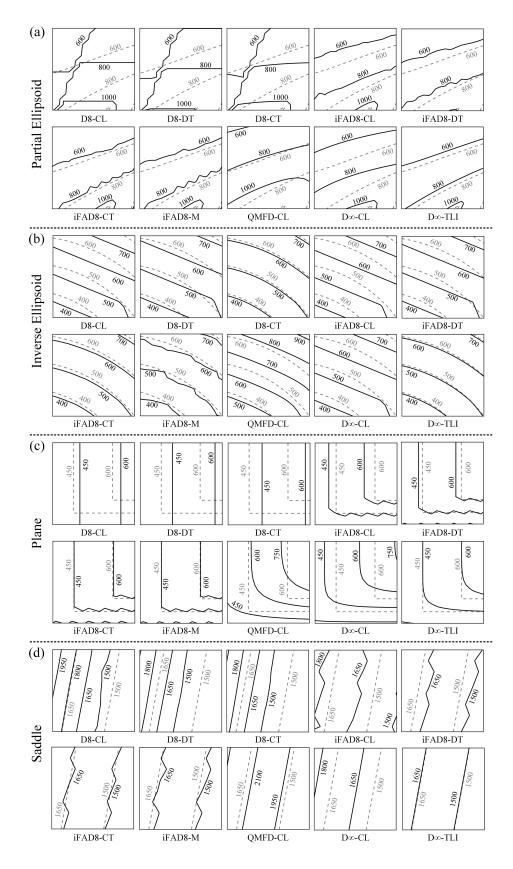
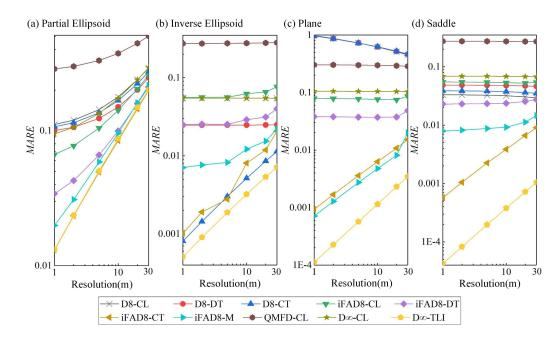


Figure 3. Four numerical and two real-world terrains are used for the assessments, including (a) an ellipsoid, (b) an inverse ellipsoid, (c) a plane, (d) a saddle, (e) the SCT Basin, and (f) the DDG Basin. Local images of (g) the SCT Basin and (h) the Duodigou Basin with several selected source points mapped are used to show the branch channels or gullies. Moreover, the elevation distribution of the square partial region of the ellipsoid (-1020 m < x, y < 1020 m) used for the flow distance assessments is shown in (i).

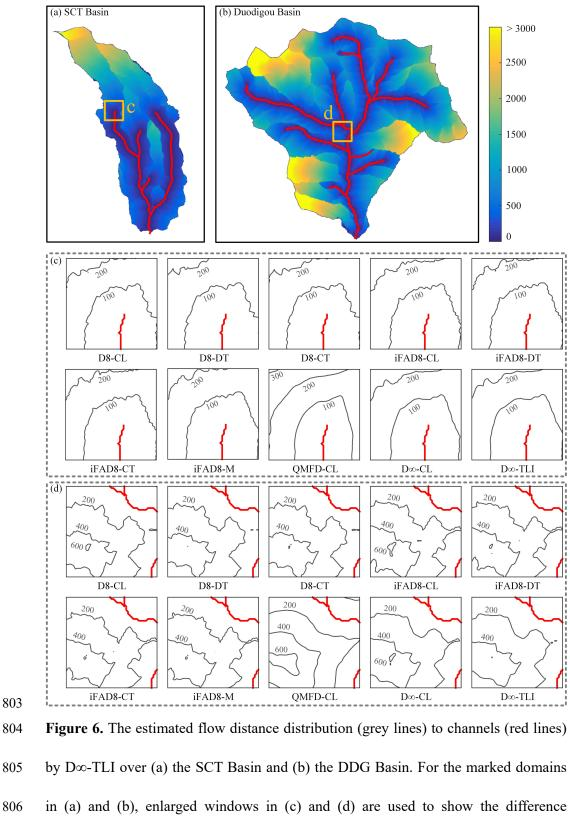


789 Figure 4. Enlarged windows of the exact flow distance distributions (grey dashed

790lines) versus estimated flow distance distributions (black solid lines) to the terrain791boundary by different algorithms over four numerical terrains with 20 m resolution.792The window ranges of the partial ellipsoid or the inverse ellipsoid are 100 m < x <793400 m and 300 m < y < 600 m. The window ranges of the plane are 350 m < x < 650794m and 100 m < y < 400 m. The window ranges of the partial ellipsoid are 150 m < x <795300 m and 1250 m < y < 1400 m.



**Figure 5.** The mean absolute relative error (*MARE*) of the estimated flow distance by different algorithms over (a) the partial ellipsoid, (b) the inverse ellipsoid, (c) the plane, and (d) the saddle with six different resolutions. Here the lines of D $\infty$ -TLI and iFAD8-CT are almost coincident for (a) the partial ellipsoid.



807 between the flow distance distributions estimated by ten selected algorithms.

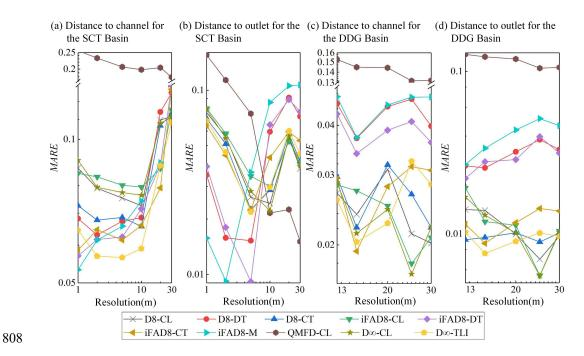


**Figure 7.** The mean absolute relative error (*MARE*) of the estimated flow distance to

810 channel or outlet for the selected points in the SCT Basin and the Duodigou Basin.

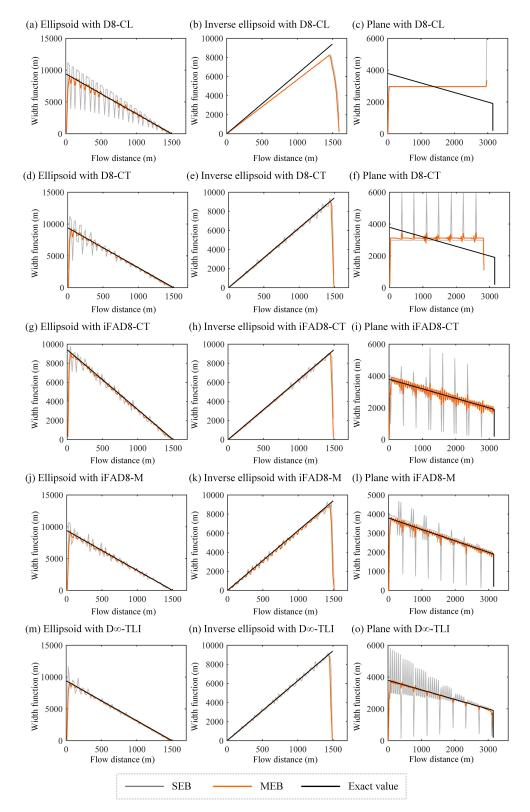
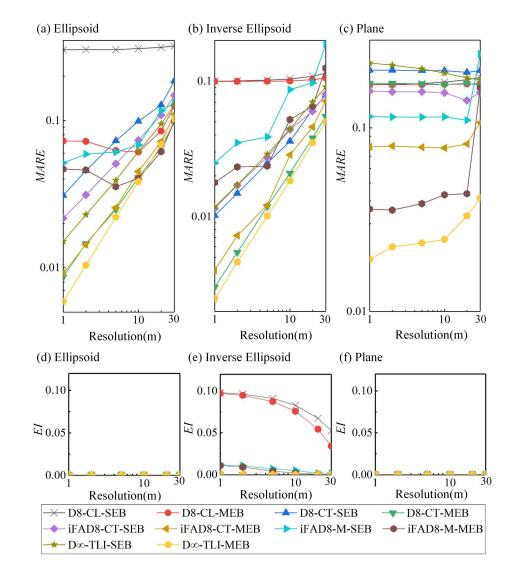


Figure 8. The width functions derived by the SEB and the MEB method with five selected flow distance algorithms and 20 m-resolution numerical terrains. The flow distance interval is equal to the resolution.





817 Figure 9. The mean absolute relative error (MARE) and the exceeding index (EI) of

the estimated width function over three numerical terrains with different resolutions.

819 The flow distance interval is equal to the specific resolution.

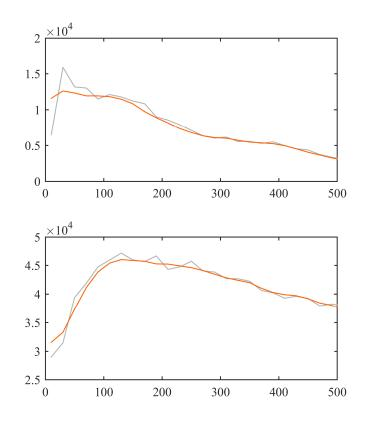
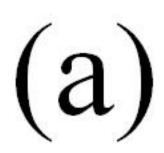
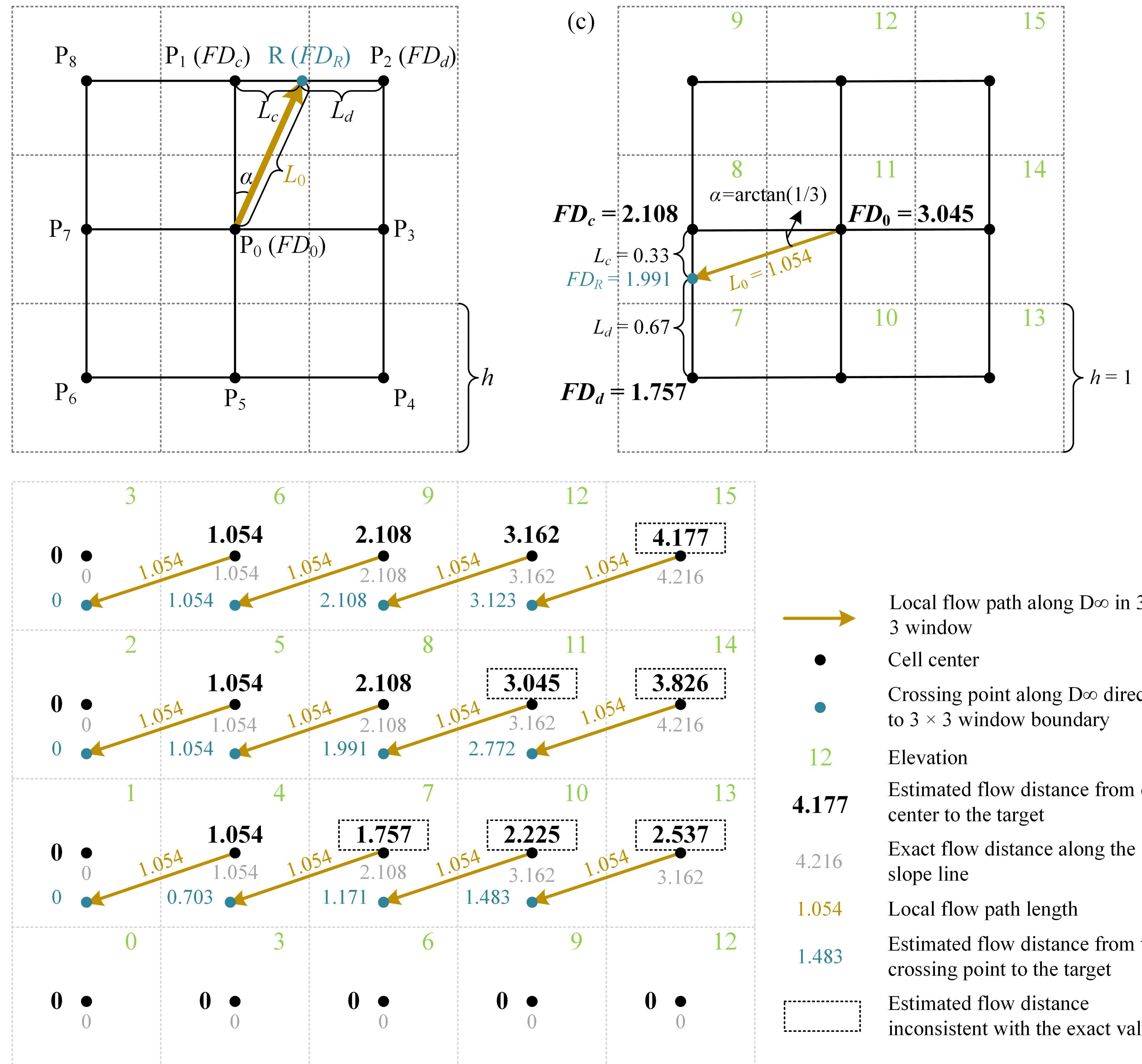


Figure 10. The partial width functions with flow distance shorter than 500 m by the SEB and the MEB method. The distributions of flow distance to channel are estimated by  $D\infty$ -TLI over (a) the SCT Basin and (b) the DDG Basin with the resolution of 20 m. The flow distance interval of the width function is equal to 20 m.

Figure 1.





- Local flow path along  $D\infty$  in 3  $\times$
- Crossing point along  $D\infty$  direction to  $3 \times 3$  window boundary
- Estimated flow distance from cell

- Estimated flow distance from the
- inconsistent with the exact value

Figure 2.

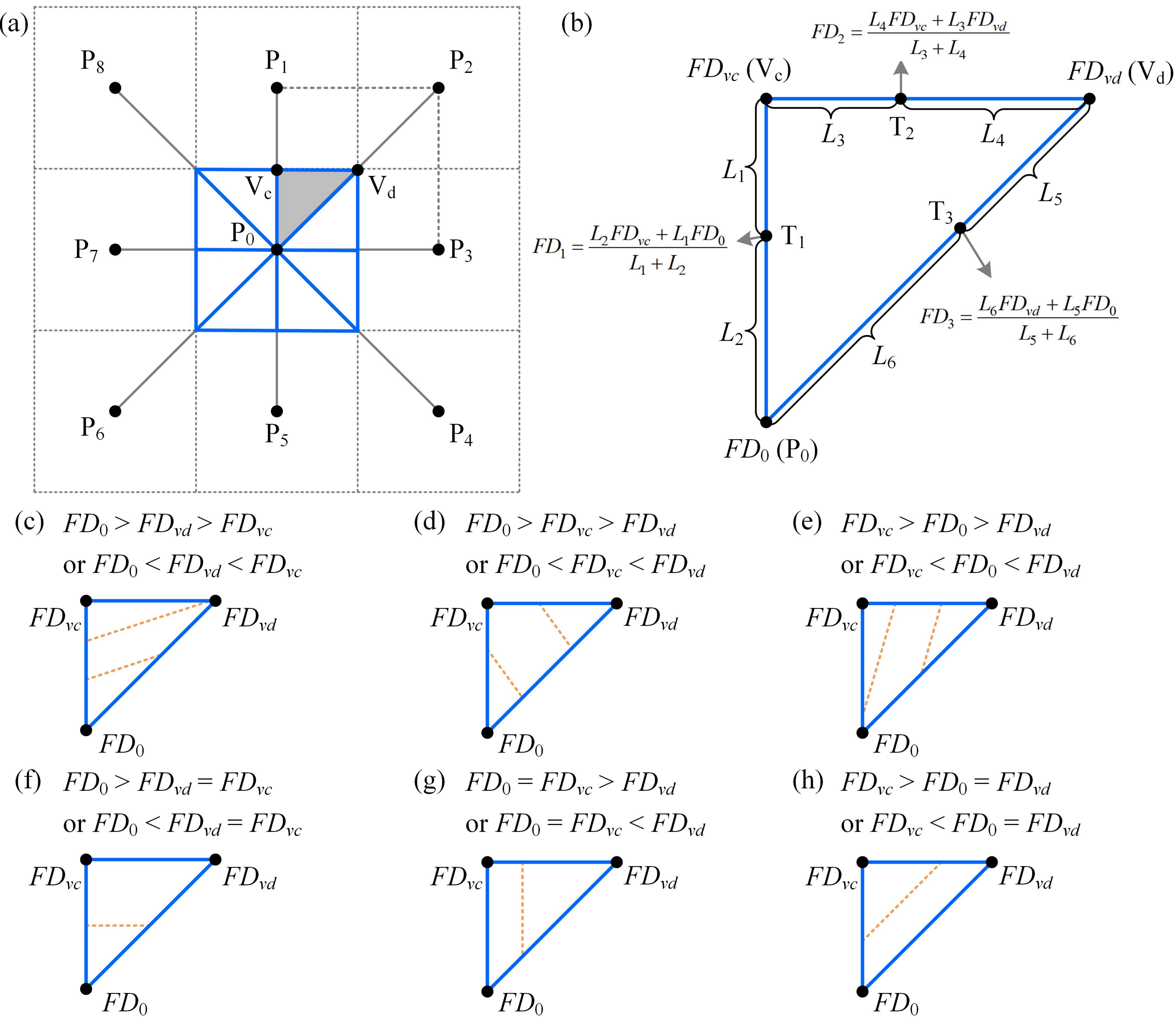


Figure 3.

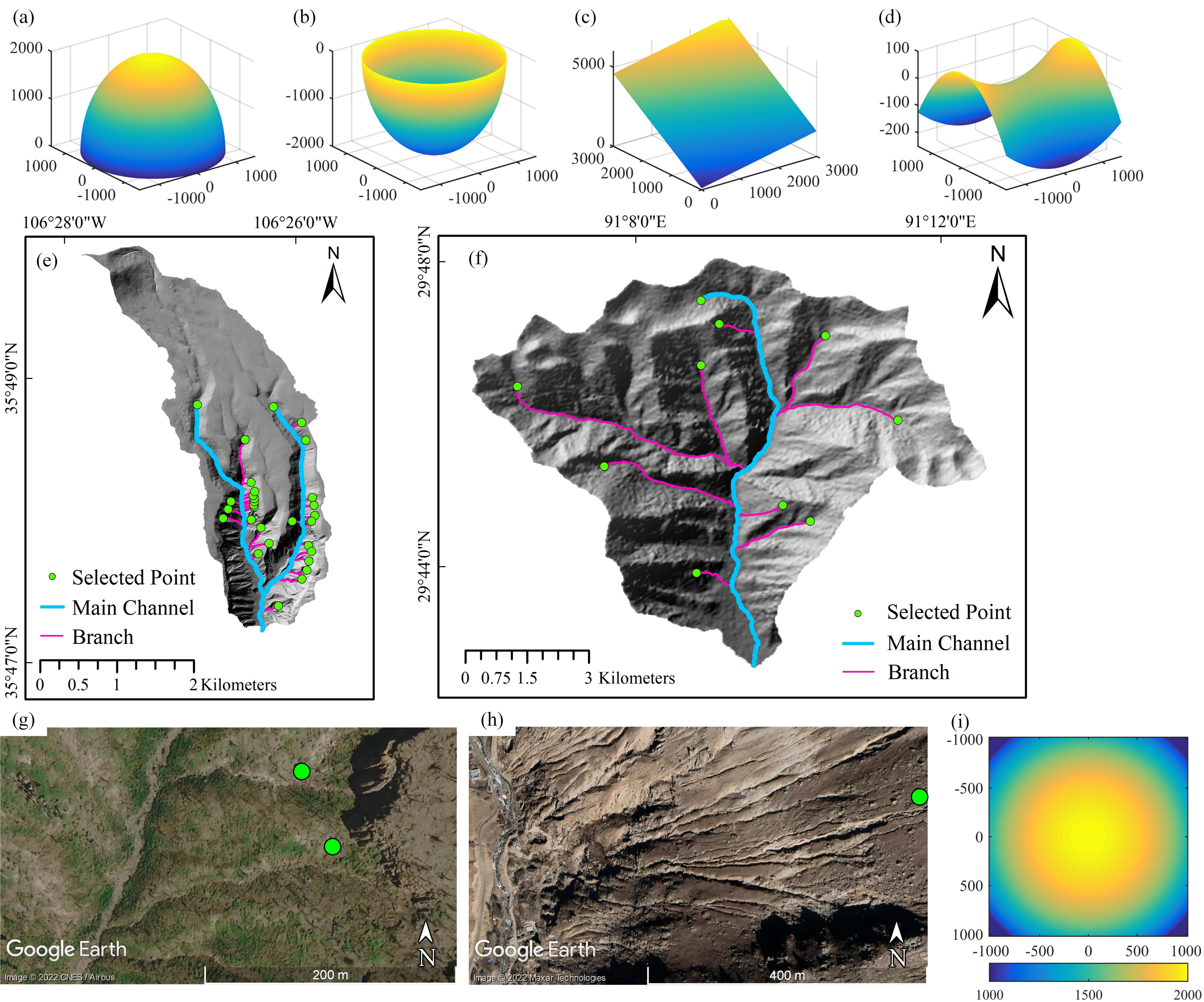
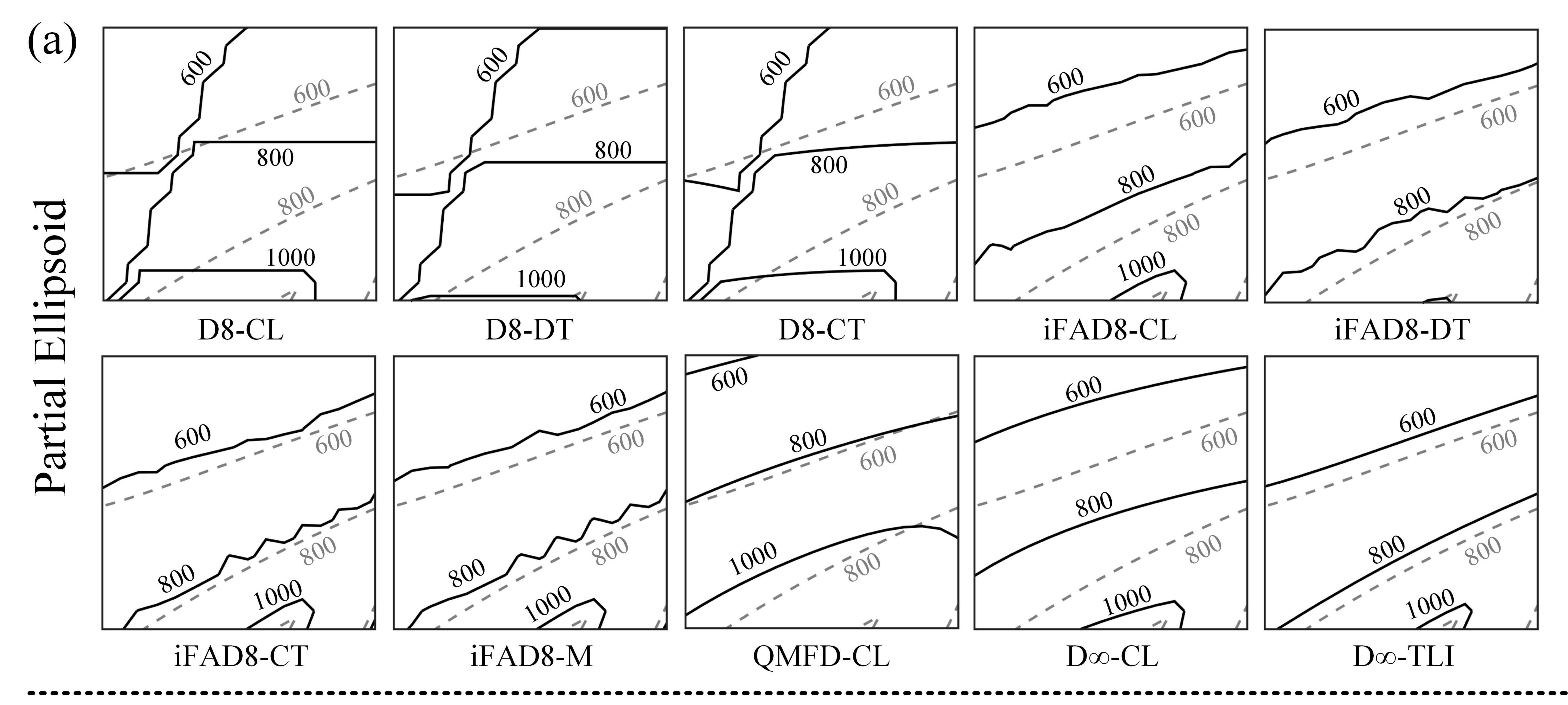


Figure 4.



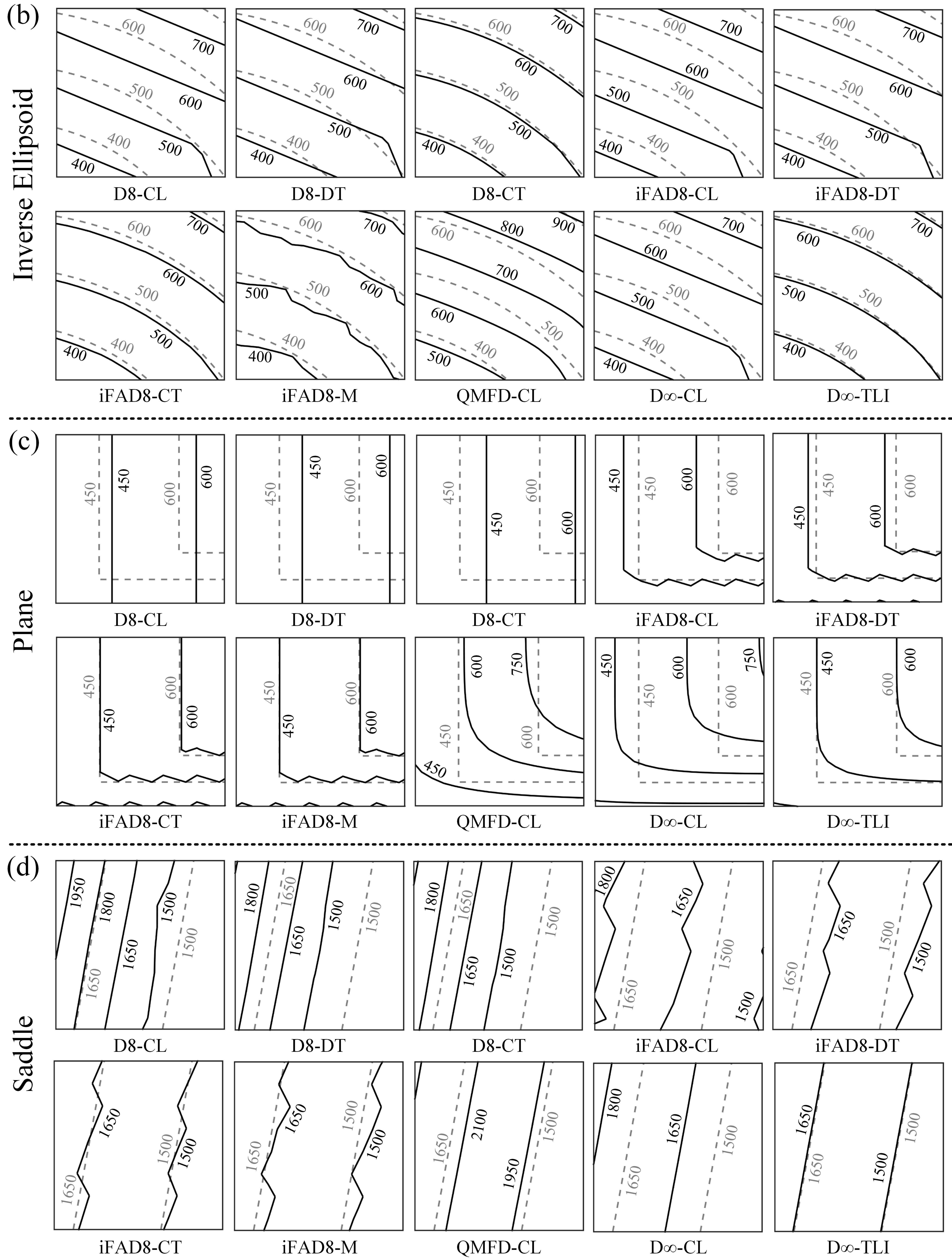


Figure 5.

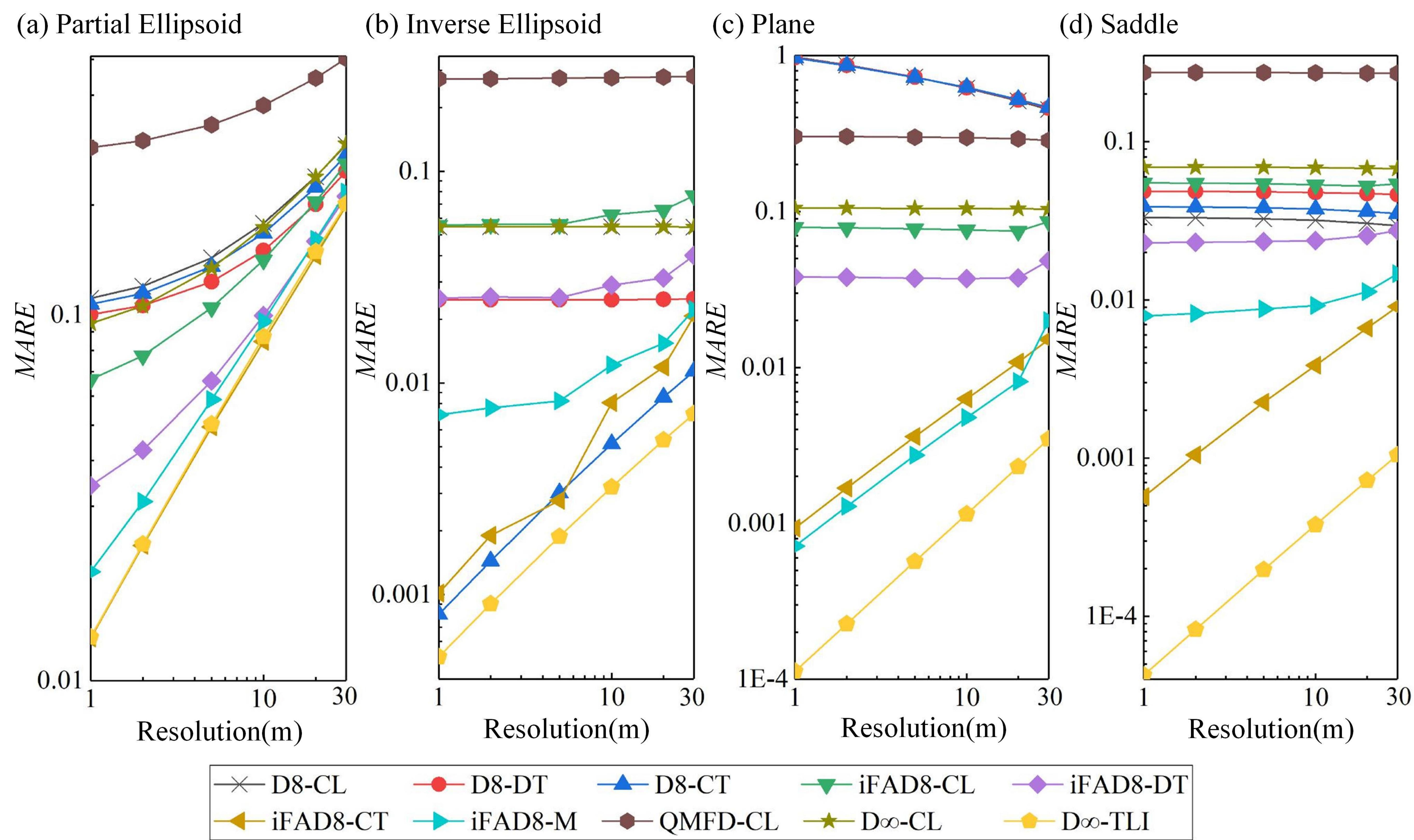
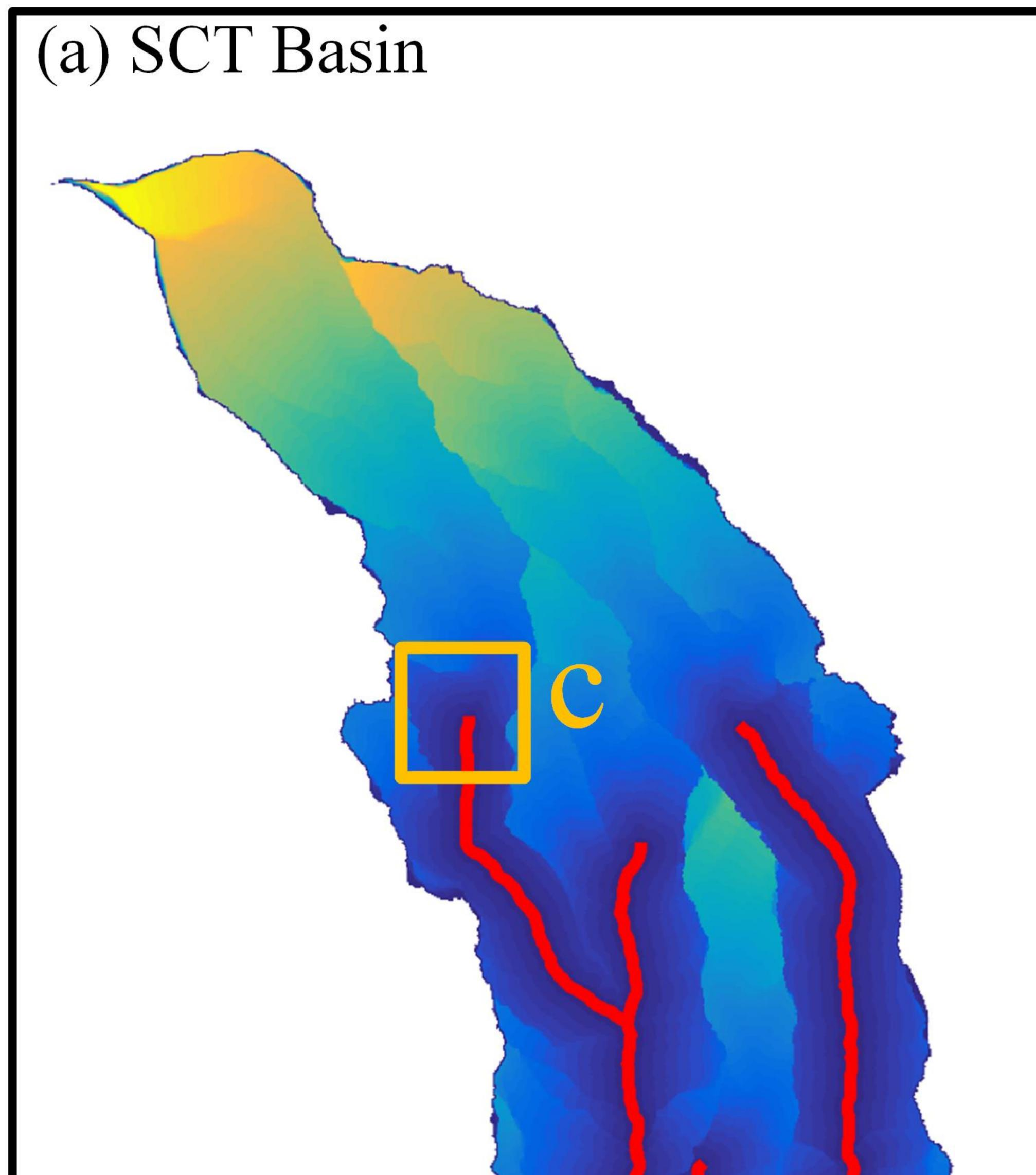
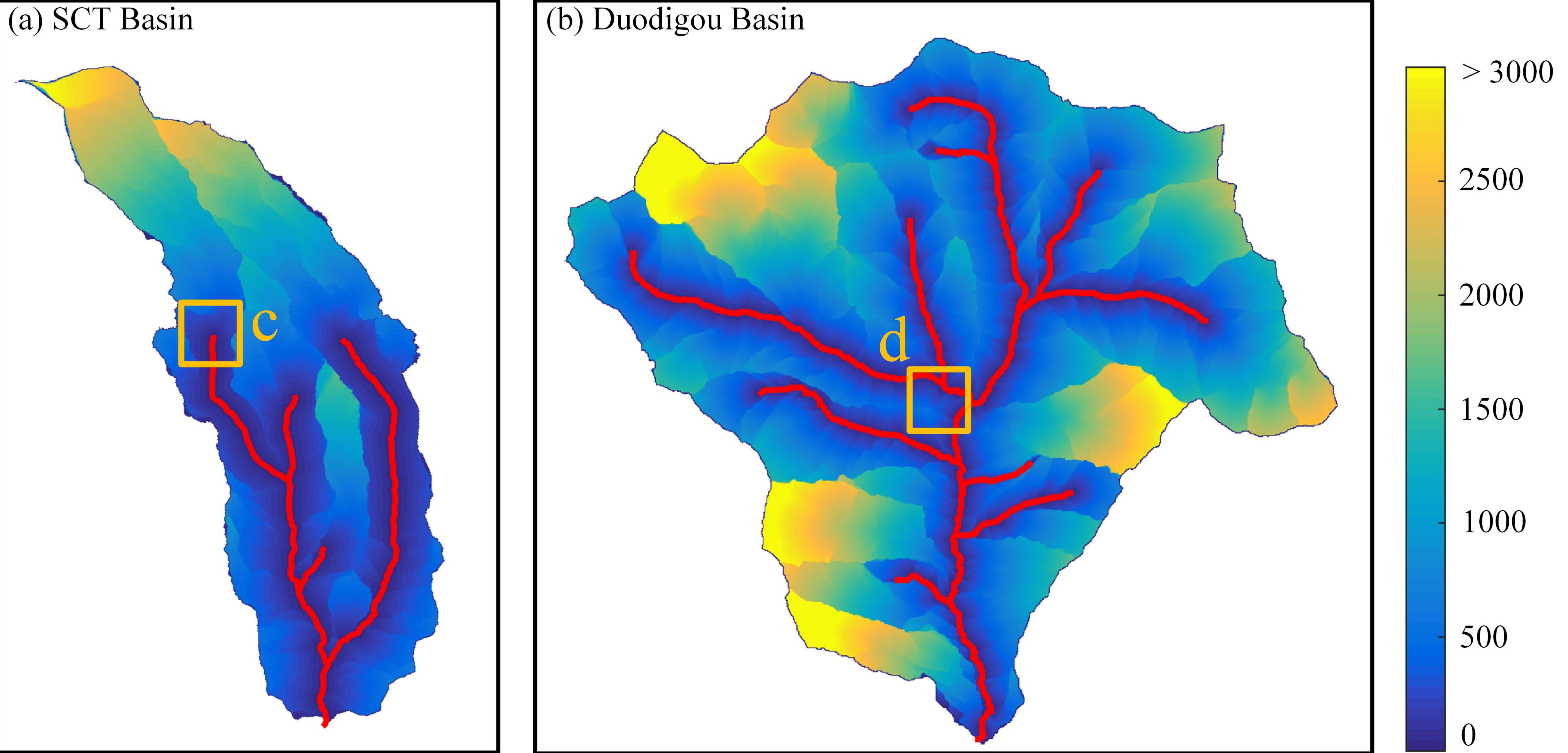


Figure 6.





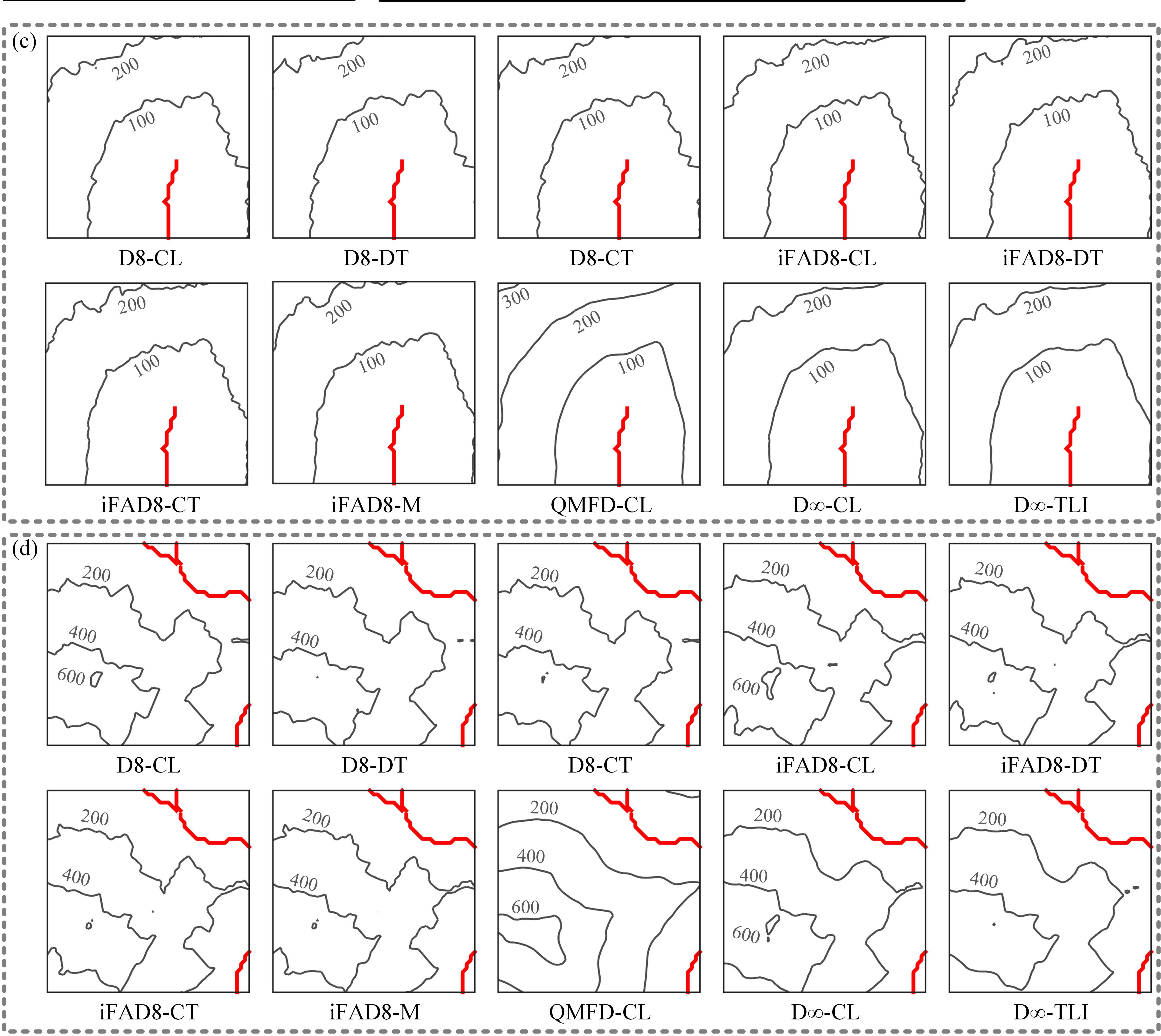


Figure 7.



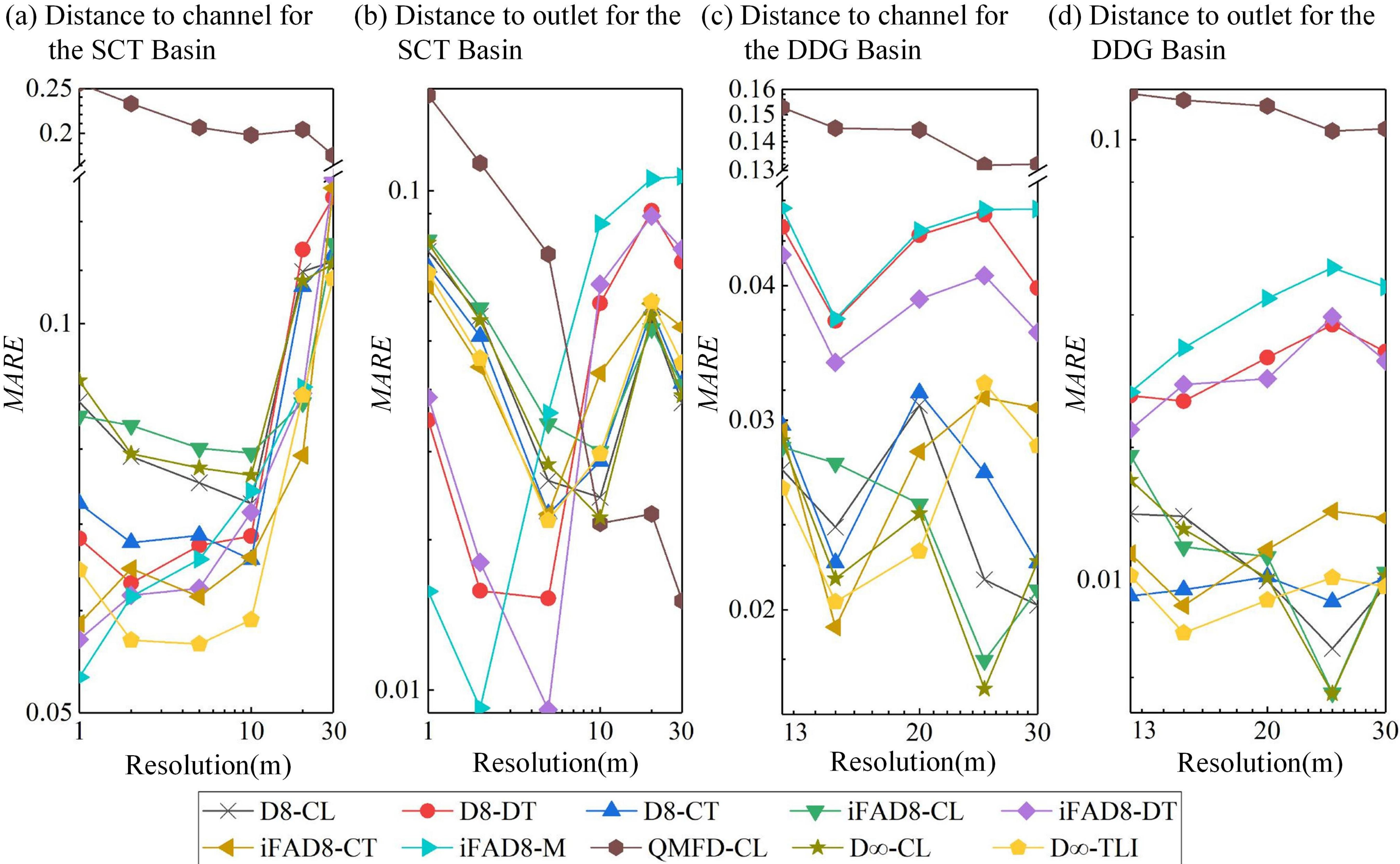
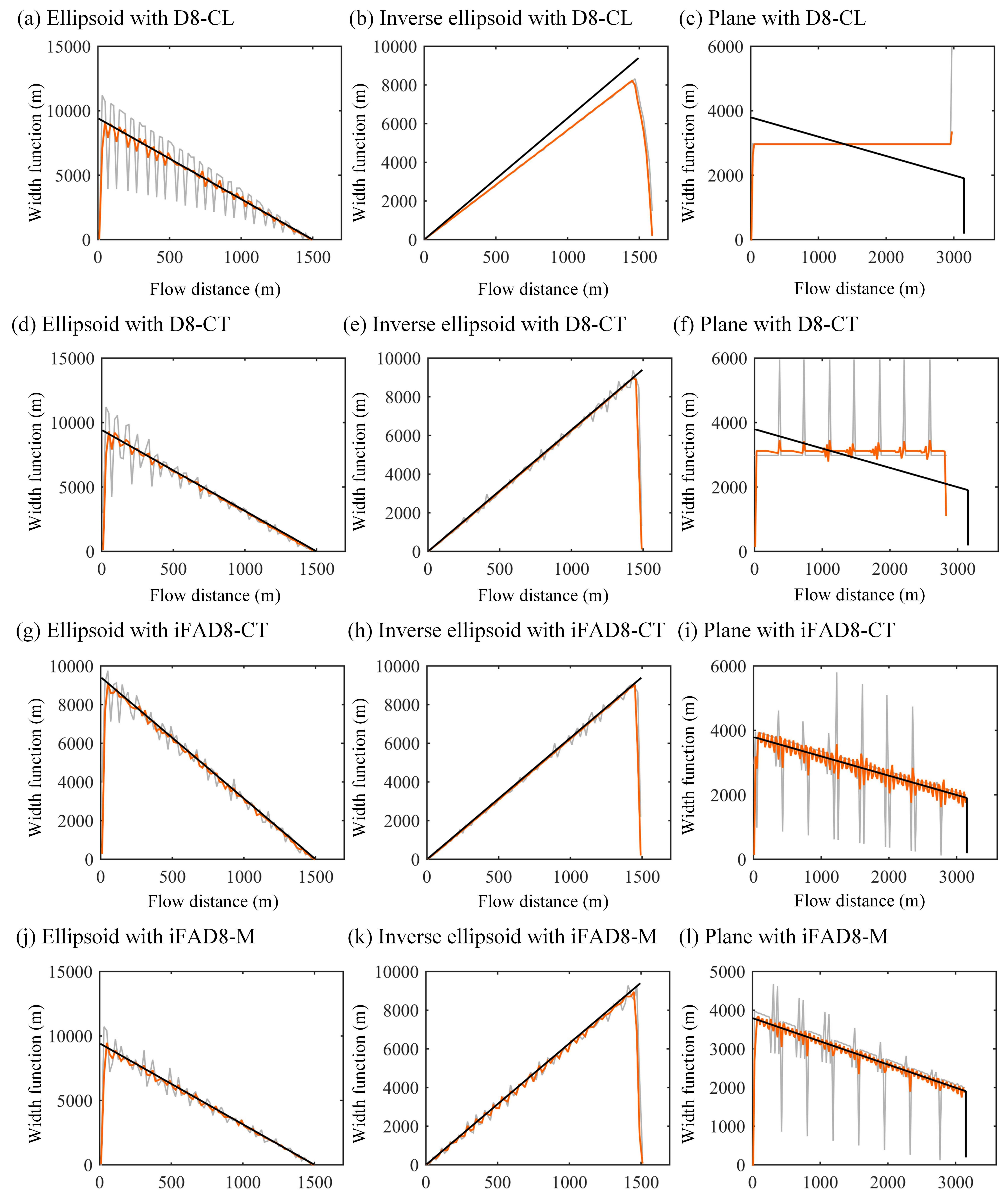


Figure 8.



Flow distance (m)

Flow distance (m)

Flow distance (m)

(m) Ellipsoid with D∞-TLI

(n) Inverse ellipsoid with  $D\infty$ -TLI (o) Plane with  $D\infty$ -TLI

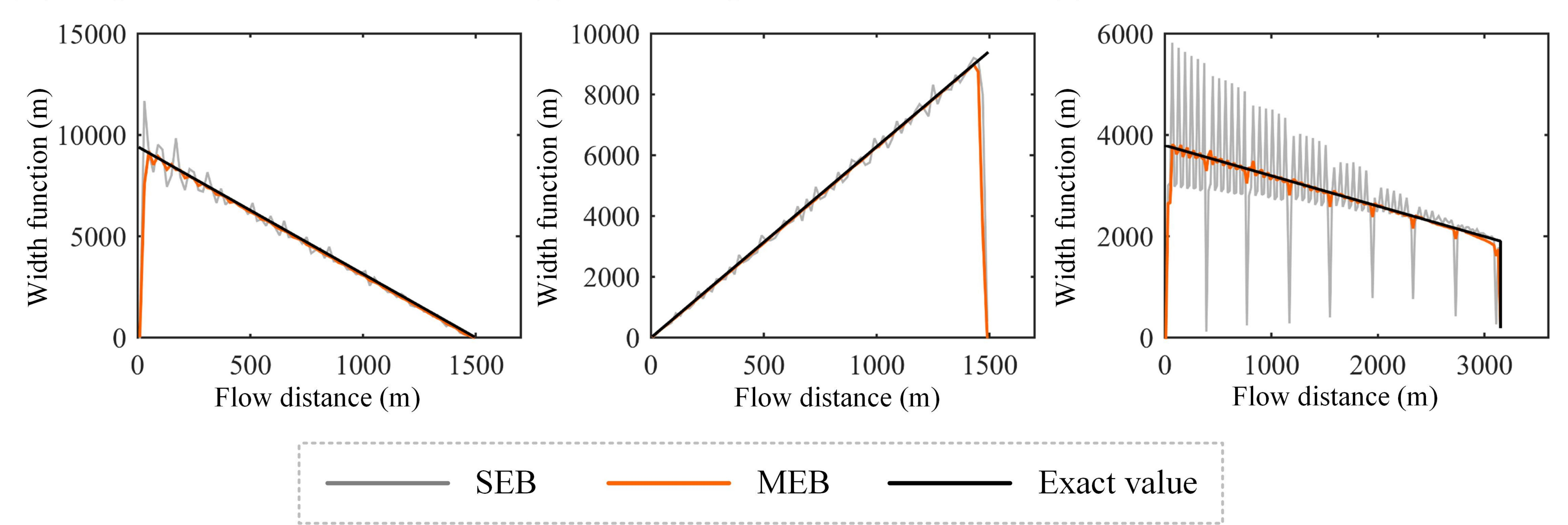


Figure 9.

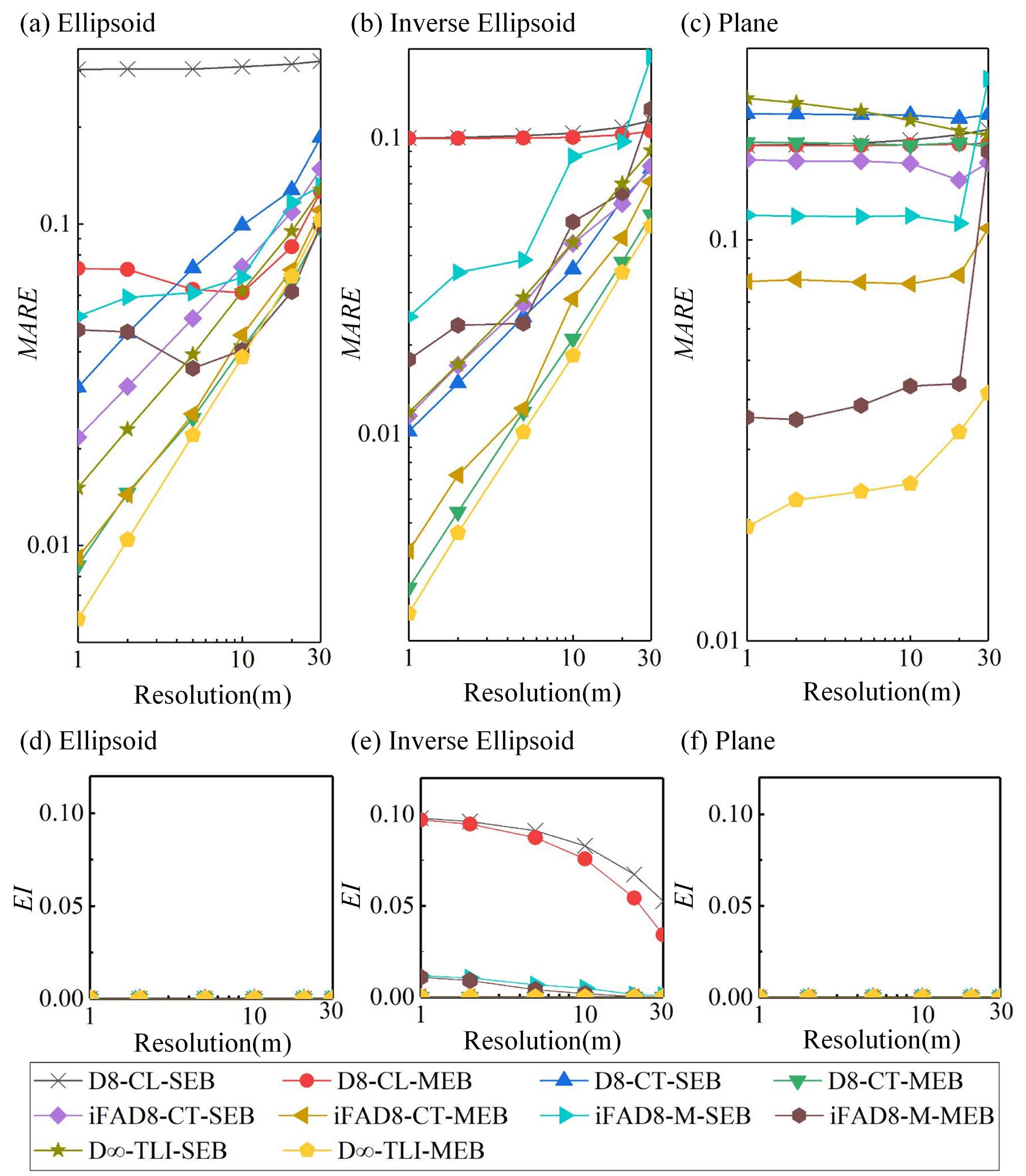


Figure 10.

